

Pushing the Limit of Asteroseismic Detection for Cool Dwarfs using TESS and Deep Learning

WALY M Z KARIM,^{1,2} ROCIO KIMAN,² DEREK BUZASI,³ CECILIA GARRAFFO,^{4,5} JOSHUA D. WING,⁴ JIM FULLER,⁶
BENJAMIN J. RICKETTS,^{7,8} VIKTOR KHALACK,⁹ AND SAJIA SHAHRIN NEHA^{10,2}

¹*Department of Physics, University of Rochester, Rochester, NY 14627, USA*

²*Department of Astronomy, California Institute of Technology, Pasadena, CA 91125, USA*

³*Department of Astronomy and Astrophysics, University of Chicago, 5801 S. Ellis Ave., Chicago, IL 60637, USA*

⁴*Center for Astrophysics — Harvard & Smithsonian, 60 Garden Street, Cambridge, MA 02138, USA*

⁵*Institute for Applied Computational Science, Harvard University, 33 Oxford St., Cambridge, MA 02138, USA*

⁶*TAPIR, Mailcode 350-17, California Institute of Technology, Pasadena, CA 91125, USA*

⁷*Anton Pannekoek Institute, University of Amsterdam, Science Park 904, Amsterdam, 1098 XH, Netherlands*

⁸*SRON, Niels Bohrweg 4, Leiden, 2033 CA, Netherlands*

⁹*Université de Moncton, 18 Antonine-Maillet Ave, Moncton, NB E1A 3E9, Canada*

¹⁰*Department of Astrophysical Sciences, Princeton University, Princeton, NJ 08544*

(Received February 1, 2026; Revised May 14, 2026; Accepted May 22, 2026)

Submitted to The Astrophysical Journal

ABSTRACT

Asteroseismology provides a powerful probe of stellar interiors by detecting stellar oscillations, including solar-like oscillations, which are stochastically excited by near-surface convection. While thousands of solar-like oscillators have been identified in evolved stars, only a limited number of main-sequence cool dwarfs have confirmed oscillations due to the low amplitudes of their signals. In this work, we train a convolutional autoencoder on TESS two-minute light curves to automatically identify solar-like oscillation features in cool dwarf main sequence and sub-giant stars. Using catalogs of confirmed oscillators for training and validation, our network achieves a classification accuracy of 99.8% on the test set, along with Precision of 0.945, Recall of 0.998, and F1 Score of 0.971. From the Asteroseismic Target List, our model identifies 3463 potential solar-like oscillators (probability > 50%). After further analysis, we find a list of 24 candidate stars that have the potential to exhibit solar-like oscillations. Notably, several of these candidates occupy regions of the color–magnitude diagram that are accessible only through more resource-intensive radial velocity observations, thereby has the potential of extending the detection frontier of TESS-based asteroseismology. Our candidate catalog provides a valuable foundation for follow-up efforts aimed at expanding the sample of cool-dwarf solar-like oscillators. This will ultimately improve our understanding of stellar structure and evolution across the lower main sequence and strengthen the evidence for using deep learning techniques to study stellar light curves.

Keywords: Late-type stars, Asteroseismology, Convolutional neural networks, Variable stars, Time domain astronomy

1. INTRODUCTION

Asteroseismology, the study of stellar oscillations, provides a powerful means to probe the internal structure and dynamics of stars (J. Christensen-Dalsgaard & S. Frandsen 1983). Recent progress in photometric time-series observation following space-based telescopes like

the Wide-Field Infrared Explorer (WIRE, H. Bruntt & D. L. Buzasi 2006), the Microvariability and Oscillations of Stars mission (MOST, G. Walker et al. 2003), the Convection, Rotation, and planetary Transits telescope (CoRoT, A. Baglin et al. 2006), Kepler (D. G. Koch et al. 2010), and the Transiting Exoplanet Survey Satellite (TESS, G. R. Ricker et al. 2015) has revolutionized the field of asteroseismology and revealed fundamental properties of thousands of stars (e.g., T. S. Metcalfe et al. 2014; Y. Lebreton & M. J. Goupil 2014; N. La-

garde et al. 2015; J. Yu et al. 2018; M. Yıldız et al. 2019). These missions have made several important asteroseismic discoveries, ranging from measuring global oscillation parameters of stars in different parts of the H-R diagram to obtaining fundamental stellar properties of metal-poor stars in our galaxy (M. Hon et al. 2021; C. Marasco et al. 2025; D. Huber et al. 2010; T. S. Metcalfe et al. 2012; F. Anders et al. 2016; M. Valentini et al. 2016). Depending on the type of oscillation, these pulsating stars occupy different regions of the H-R diagram. Solar-like oscillators appear on the cool main sequence and red-giant branch, whereas classical pulsators such as δ Scuti, RR-Lyrae, and Cepheids lie along the instability strip. The low oscillation amplitudes of low-mass main sequence stars, particularly in the late K dwarfs and M dwarfs, have restricted the previous attempts to find oscillation signals in them (W. M. Z. Karim et al. 2025; C. Rodríguez-López et al. 2014; C. Rodríguez-López 2019).

G and K dwarfs primarily exhibit solar-like oscillations, while M dwarfs have been theorized to exhibit similar oscillation features (C. Rodríguez-López et al. 2012; T. L. Campante et al. 2024; E. Hatt et al. 2023). Solar-like oscillations contain sequences of radial overtones that are stochastically excited by turbulent convection close to the stellar photosphere. They can be broadly characterized by two main global parameters: the frequency of maximum power (ν_{\max}) and the large frequency separation ($\Delta\nu$). ν_{\max} describes the central frequency of the visible Gaussian envelope like power excess, and $\Delta\nu$ describes the approximately regular spacing between consecutive radial overtones for a given angular degree. A precise measurement of these oscillation parameters, combined with an independent measurement of the effective temperature, can be used to identify fundamental properties such as stellar mass, radius and age, with high accuracy (e.g., T. S. Metcalfe et al. 2010; V. Silva Aguirre et al. 2012; D. Huber et al. 2012; E. Guggenberger et al. 2016; P. Gaulme et al. 2016; S. Mathur et al. 2022).

Any star having a near-surface convection zone can excite solar-like oscillations. Hence, this type of variability has been observed in the main-sequence (e.g., W. J. Chaplin et al. 2014b), sub-giant (e.g., T. Appourchaux et al. 2012; S. Mathur et al. 2022) and red giant (e.g., T. R. Bedding et al. 2010; J. Yu et al. 2018) branches of the H-R diagram. However, there have only been a handful of detections of solar-like oscillators in cool main sequence stars ($T_{\text{eff}} < 5500$ K) due to their low luminosity and small oscillation amplitudes (S. Hekker 2019; T. L. Campante et al. 2024; S. Mathur et al. 2019; E. Hatt et al. 2023). The probability of detecting solar-

like oscillation in these part of the H-R diagram is further complicated by the fact that the least evolved stars have oscillation frequencies in the range from $10^3 \mu\text{Hz}$ to $10^4 \mu\text{Hz}$, which is close to the Nyquist limit of Kepler and CoRoT based photometry (J. M. Benkő et al. 2016; S. J. Murphy et al. 2013). All of these constraints combined have resulted in only of order ~ 100 solar-like oscillators in the main sequence and sub-giant branch which are colder than the Sun (E. Hatt et al. 2023; T. L. Campante et al. 2024; T. Arentoft et al. 2008; S. Mathur et al. 2017; H. Kjeldsen et al. 2008), compared to of order $\sim 10^5$ red giant solar-like oscillators detected in a single study in M. Hon et al. (2021).

TESS provides a unique opportunity to detect high-frequency, low-amplitude stellar oscillations owing to its short observing cadence, as low as 20 seconds as opposed to 1 min for Kepler, and its sensitivity at red optical wavelengths. TESS maximizes sky coverage by observing the sky in sectors, with individual targets typically monitored in multiple sectors. Each sector spans approximately 27.4 days, yielding light curves with baselines long enough to probe oscillatory signals in main sequence stars (M. N. Lund et al. 2025). During the nominal mission, TESS delivered light curves at 2 min cadence, corresponding to a Nyquist frequency of $4167 \mu\text{Hz}$, while the extended mission introduced a 20-second cadence mode, pushing the Nyquist limit to $25,000 \mu\text{Hz}$. These capabilities make TESS exceptionally well-suited for detecting high-frequency, solar-like oscillations in cool dwarfs. However, exploiting the full potential of such high-quality data requires searching oscillations across large samples of stars.

Because solar-like oscillations are stochastically excited and intrinsically variable from star to star, constructing a general parametric model is challenging. For a list of existing parametric models (See D. Huber et al. 2009; S. Mathur et al. 2010; A. Chontos et al. 2022; B. Mosser et al. 2012; M. B. Nielsen et al. 2025). Existing parametric approaches are primarily designed to extract seismic parameters once oscillations have been confirmed, rather than to detect their presence in the first place. This motivates the need for techniques that capture the characteristic features of solar-like oscillators while remaining robust to stochastic variability. One such example can be found in D. Huber et al. (2009) where the authors used an automated approach to calculate autocorrelation functions of power spectrum to look for signs of oscillations. However, it also required a final manual evaluation of each object, making it impractical for searching over a large catalog.

Deep learning offers an effective alternative for efficiently searching large datasets to identify solar-like os-

cillations. Recently, deep learning techniques have been widely adopted in astronomical classification problems both in time series and frequency domain (e.g., A. Mahabal et al. 2017; B. Naul et al. 2017; S. Jamal & J. S. Bloom 2020; S. Bassi et al. 2021; F. Pérez-Galarce et al. 2025; C. Aguirre et al. 2018; I. Becker et al. 2020; K. Zhang & J. S. Bloom 2021; M. Abdollahi et al. 2022; J. Audenaert et al. 2021, 2025). By training on known solar-like oscillators, a neural network (NN) can learn the underlying signal morphology and subsequently be applied to identify candidate oscillations in new targets as demonstrated by M. Hon et al. (2018), to find solar-like oscillation in red giants using Kepler.

Despite these advances, contemporary architectures present practical limitations for detecting solar-like oscillations in TESS data. Many state-of-the-art models (e.g., B. Naul et al. 2017; S. Jamal & J. S. Bloom 2020) assume fixed-length or phase-folded inputs (or segment long light curves into fixed-length slices), an approach that is problematic for TESS sector data: a single 27.4-day sector sampled at 2 min cadence contains around 2×10^4 measurements (and about 1×10^5 measurements for a 20-second cadence sector). Thus, forcing fixed-length inputs typically requires aggressive rebinning, which reduces sensitivity to high-frequency signals, or segmentation, which reduces oscillation amplitude since we are using the Lomb-Scargle periodogram (N. R. Lomb 1976) where amplitude can depend on the segment size (J. T. VanderPlas 2018). Also, phase folding does not reveal the oscillation features for solar-like oscillators (see Section 2.1). In contrast, periodograms cleanly separate the broadband granulation background from the oscillation power excess: the former is well described by Harvey-like/super-Lorentzian components and a low-frequency slope, while the latter appears as a Gaussian-like envelope centered near ν_{\max} (e.g., T. Kallinger et al. 2014; B. Mosser et al. 2012). Detecting new solar-like oscillators therefore reduces to learning these two spectral signatures, a task well suited to convolutional architectures that can recognize spatial patterns with high accuracy. This approach was pioneered for red giants by M. Hon et al. (2018), who trained Convolutional Neural Networks (CNN) on log-scale power-spectrum images to detect oscillation power excess with human-level performance. In this study, we modify this technique to find pulsation in main-sequence and sub-giant stars.

In this work, we present the first deep-learning study specifically targeting solar-like oscillations in cool main-sequence and sub-giant dwarfs using TESS 2 min cadence data. In our study, we have found very promising candidates in M, K, and G dwarf regions of the color-

magnitude diagram. Although we do not claim any detection, these candidates could be verified in follow-up observational efforts. We trained a one-dimensional convolutional autoencoder that learns a compressed representation (also known as a latent space) of stellar periodograms. This latent space representation is coupled to a classifier head that distinguishes solar-like oscillators from a broad comparison set of other types of stellar variability, including other types of pulsators that do not exhibit solar-like oscillations such as δ Scuti, RR-Lyrae, and Cepheids. We then applied the trained network to a sample of around 91,000 stars cooler than G0, selected from the Asteroseismic Target List (ATL, D. Hey et al. 2024). Candidate detections were subsequently validated with pySYD (A. Chontos et al. 2022), which provided global asteroseismic parameters and diagnostic plots to confirm the variability source. To give a brief outline of this paper, we discuss our sample selection and data pre-processing in Section 2, and then introduce the architecture and training process of the neural network in Section 3. In Section 4, we discuss the target and candidate selection process and the various cuts we considered to make our candidate list, along with a comparison with previously detected solar-like oscillators. In Section 5, we present the most interesting objects in our list of candidates, followed by our conclusions in Section 6.

2. DATA

To train our neural network, we used periodograms instead of a more conventional light curve approach, and Section 2.1 is dedicated to justify this choice. We have also constructed a comprehensive training set composed of two main samples: 4,177 previously identified solar-like oscillators and 82,204 stars representing other types of pulsators, variable stars, and non-variable sources. Each of these samples is described in detail in Section 2.2 and Section 2.3, respectively. In Section 2.4, we also describe the processing steps used to transform these samples into a suitable training dataset.

2.1. Light Curves versus Periodograms

There are four standard representation of stellar light curves that can be used as inputs for neural network classification: full time-series, segmented time series, phase-folded light curves, and periodograms. We experimented with all four representations and chose to proceed with the periodogram-based approach for the remainder of our analysis. Below, we justify this choice by discussing the properties of each representation and the advantages of periodogram-based classification.

S. Bassi et al. (2021) and U. F. Burhanudin et al. (2021) used raw time series data to classify variable

sources. The time series used in this study consisted of only 100 and 30 epochs respectively. However, TESS 2 min cadence data has a longer baseline, consisting of $\sim 15,000$ points. Training a neural network with such a large input layer is computationally expensive and impractical.

The second method consists of phase folded light curves, as explored by [B. Naul et al. \(2017\)](#) and [S. Jamal & J. S. Bloom \(2020\)](#) where this technique has shown to reach up to 99% and 97% accuracies respectively. However, to phase fold the light curve, one needs to know the period of variability beforehand, which is often hard to accurately determine. Also, we have noticed that the phase folding on one frequency does not reveal a consistent oscillatory pattern because more than one oscillation mode is stochastically excited. [Figure 1](#) shows an example where a light curve for a solar-like oscillator has been folded on the ν_{\max} ([E. Hatt et al. 2023](#)), and there is no noticeable variability pattern in the folded light curve.

A third approach is to split the long baseline of the light curves into segments of smaller lengths, and have overlapping segments to create a running window effect that preserves the phase information. However, as discussed in [B. Naul et al. \(2017\)](#), if the light curves have high frequency variation in brightness, the neural network’s ability to learn these variability patterns deteriorates significantly. We have also tried the approach of splitting the light curves into distinct segments without creating the running window effect. However, given the length of TESS 2 min cadence light curves, each light curve was split into 5 - 6 distinct signals, which made our training set 5 - 6 times larger. This resulted in slower training convergence, and the classification accuracies were low as well (about 80%).

The last approach is using the periodogram. The periodogram has the advantage that binning it to a smaller length does not remove the signal for any frequency range as long as it is not too aggressive. Also as our goal is to identify solar-like oscillators, and these have a particular shape in the periodogram ([Figure 2](#)), we found that it is the most efficient way to distinguish them. The NN can learn to find those features to distinguish our target signals from the others. Therefore, we decided to use a 1D periodogram, and re-bin it in logarithmic scale (which is equivalent to a log-log periodogram) to a fixed length of 4096 points to train our model.

2.2. Solar-like Oscillators

We trained our model on a set of previously identified solar-like oscillator to make it learn and recognize their periodogram shapes. The sample of solar-like os-

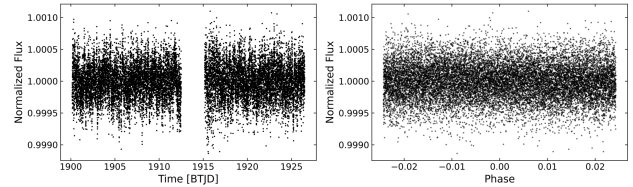


Figure 1. Light curves of solar-like oscillator before and after phase folding on its ν_{\max} . Left panel shows the raw light curves and right panel shows light curve after phase folding.

cillators was obtained from [E. Hatt et al. \(2023\)](#) which consists of 4177 manually verified solar like oscillators (SOLR) from TESS 120-s and 20-s cadence data. The authors used a detection algorithm based on finding power-excess and regularly spaced radial overtones in the power-spectrum, followed by a manual verification of each candidate. This resulted in 3691 solar-like oscillators in 120-s cadence and 486 SOLR in 20-s cadence. The distribution of frequencies of maximum amplitude, ν_{\max} of this sample ranges between $\sim 10 \mu\text{Hz}$ to $\sim 3000 \mu\text{Hz}$. Some of the SOLR from [E. Hatt et al. \(2023\)](#) were found using 20 second cadence that do not show oscillations in 2 min light curves. We decided to remove these objects for uniformity across our training sample.

Most SOLR power spectra are characterized by a granulation-dominated slope at low frequencies, followed by a Gaussian-shaped envelope of excess power arising from stellar oscillations ([M. Hon et al. 2018](#)). An example is shown in [Figure 2](#), which just serves the purpose of schematic illustration, and does not serve any quantitative purpose. In the plot, the granulation component is highlighted in red, and the oscillation hump is clearly visible near the frequency of maximum power, indicated by a vertical dashed blue line. These two distinct features are visually most apparent in log-log space, which makes it easily identifiable by a Convolutional Neural Network because the log-log scaling emphasizes the characteristic shapes of the granulation background and oscillation hump. Therefore, we bin our periodograms logarithmically before passing them to the neural network. This type of periodogram representation was first used by [M. Hon et al. \(2018\)](#) to identify red giant oscillations, where the data were treated as 2D images in logarithmic space. In contrast, we adopt a 1D representation, which is significantly less computationally expensive while still preserving the relevant morphological information. Our deep learning model is trained to learn and recognize this characteristic shape (see [Section 3](#)) and is subsequently applied to search for oscillations in stars of previously unknown types (see [Section 4](#)).

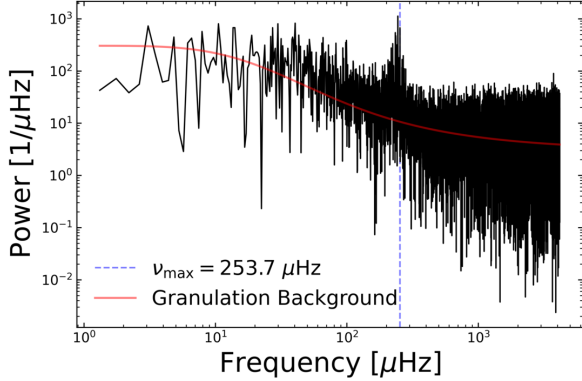


Figure 2. Power Spectrum of a solar-like oscillator of an evolved star with TIC 141201954. Granulation background fit is in red and oscillation power excess frequency is marked in a blue vertical dashed line. **The figure is just for schematic illustration, and does not serve any quantitative purpose.**

Table 1. Number of stars per class of light curve in our training and test sample combined.

SOLR	NonSOLR			
	PULS	ROT	EB	NV
4177	15200	24688	5796	36520

NOTE—The SOLR column refers to the sample of known solar-like oscillators. The NonSOLR type consists of four variability classes: Pulsators (PULS) that are not solar-like, rotators (ROT), eclipsing binaries (EB), and non-variables (NV).

2.3. Non Solar-like Oscillators

We obtained the sample of stars that do not show solar-like oscillations from [L. A. Balona \(2023\)](#). This author provided visual classification of 120,000 variable stars observed by Kepler and TESS. For our sample, we selected 82,204 stars that were observed by TESS. These stars have both variable and non-variable light curves. We grouped the stars that do not show solar-like oscillations (NonSOLR) into four major classes: Pulsators (PULS), Rotators (ROT), Eclipsing Binaries (EB), and Non Variables (NV). The distribution of these four groups is shown in [Table 1](#). These four categories were chosen as true negatives for training because they are the most abundant types of variable stars that do not show solar-like oscillations ([L. A. Balona 2023](#)).

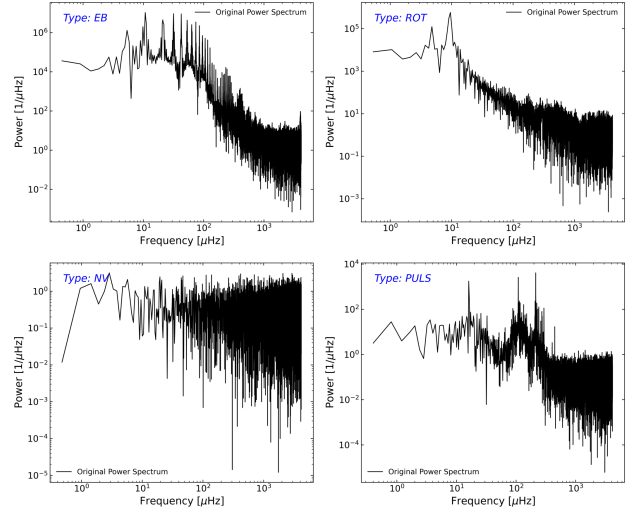


Figure 3. Example power spectrum of stars with no solar-like oscillation. Top left is eclipsing binary, and right is rotator. Bottom left is non variable and bottom right is a δ Scuti pulsator.

Figure 3 shows examples of power spectrum from stars from different variability classes that do not show any solar-like oscillations. The top left panel of the figure shows an eclipsing binary, which has a very distinct shape of multiple harmonics. The top right panel shows a rotator, with a singular low frequency peak. The bottom left panel shows a non variable star with the characteristic flat white noise, followed by a δ Scuti pulsator on the bottom right panel, with multiple peaks above 20 μ Hz. Visibly, these stars have different shapes from a solar-like oscillator (see [Figure 2](#)) since none of them have a combination of granulation slope and a gaussian-like power excess hump due to oscillations.

2.4. Pre-processing

In this section, we describe our data pre-processing techniques for both samples of SOLR and NonSOLR. First, we obtained the TIC ids of the SOLR and NonSOLR sample from the two catalogs described in [Section 2.2](#) and [Section 2.3](#).

For the SOLR dataset, we used light curves from all available TESS sectors to allow the model to learn both intrinsic signal characteristics and instrumental systematics. Each sector’s light curve was treated as an individual object, even if multiple sectors corresponded to the same star. This approach was mainly taken because for some stars, the oscillation signal becomes visible only after combining multiple sectors. However, stitching multiple sectors is known to produce systematics that might interfere with the training process ([A. W. Boyle et al. 2025](#)). It also helped us address the class imbalance be-

tween SOLR, which originally had only 4177 stars, and NonSOLR, which has 82,204 stars. After considering all sector light curves, the SOLR sample had 29,621 periodogram signals. By including all the sectors available for one star as separate stars, we are training the neural network on TESS systematics, as well as on recognizing the pulsation signal. This method is similar to the standard data augmentation technique of training a network on the same signal multiple times, but each time adding a small noise component to the signal. It has been shown to improve classification and generalization capabilities of neural network models (e.g., G. I. Kim & K. Chung 2024).

For the NonSOLR sample, we downloaded only one sector per star. We did not use any criteria in choosing a sector, but rather just downloaded the first sector the star was observed in.

For all light curves, we utilized the `lightkurve`¹¹ package to download the time series. The signals were processed by TESS Science Processing Operation Center (SPOC, J. M. Jenkins et al. 2016), which carries out simple aperture based photometry and removes any instrumental noise. Also, we only used TESS 120-s cadence light curves, since 20-s data is available for only a select number of stars, and has been shown to have different systematics than 120-s data (D. Huber et al. 2022). Once we downloaded the light curves, we cleaned it using `remove_outliers()` method which removed data points from the light curves residing beyond a 5σ deviation from the mean flux. As a next step in our pre-processing, we calculated the Lomb-Scargle periodogram using built-in `lightkurve.periodogram.Periodogram()` functionality with its default settings. These periodograms are used as the input to the NN (See Section 2.1). To facilitate identifying the shape of solar-like oscillators by the neural network, we binned the periodogram on a logarithmic scale (See Section 2.2). The network also requires all input to be of specific length, so we binned the signal to 4096 points, where this number was chosen based on trial and error. Logarithmic binning reduces the frequency resolution of the periodogram. Given the Nyquist limit of $4167 \mu\text{Hz}$, and the fact that each TESS 2 min periodogram has around 16,000 points, this binning results in a frequency resolution of about $4.7 \mu\text{Hz}$ around $2000 \mu\text{Hz}$ frequency and a resolution of around $7.1 \mu\text{Hz}$ around $3000 \mu\text{Hz}$ frequency. However, these resolutions are well above the mode separations of solar-like oscillation, which is in the order of $\sim 100 \mu\text{Hz}$. Therefore,

logarithmic binning does not pose a threat of losing the oscillation signal.

Once we obtained the signals binned to 4096 points, we used `MinMaxScaler()` function from `scipy`¹² to normalize each signal between 0 to 1. This helps the neural network to have a smooth gradient flow and converge faster. Since we are only doing a binary classification, we assigned the stars to two different classes: SOLR, which shows solar-like oscillations and NonSOLR, which does not show solar-like oscillation, but might contain other types of variability.

3. NETWORK ARCHITECTURE & TRAINING

To enable variability classification, we developed a convolutional autoencoder designed to learn characteristic periodogram morphologies of stars across different variability types. The network compresses each input periodogram into a low-dimensional latent representation of length 128. A classification head is then attached to this latent space to distinguish between two primary categories: SOLR and NonSOLR. The network architecture was developed using `PyTorch`¹³ framework in python. All network architectures and their full implementation is publicly available on GitHub¹⁴.

The complete model was trained on the sample described in the previous Sections 2.2, 2.3 and 2.4, and evaluated on an independent test set, achieving a classification accuracy of 99.8%. In this section, we present the architectural design of the neural network and discuss its training, validation, and testing performance.

3.1. Autoencoder

An autoencoder is a neural network architecture widely used for unsupervised representation learning, dimensionality reduction, and data compression (G. E. Hinton & R. R. Salakhutdinov 2006). At its core, an autoencoder is trained to reconstruct its input data, thereby forcing the model to learn compact, informative representations of complex, high-dimensional inputs. This property makes autoencoders particularly suitable for analyzing large and structured astronomical datasets, where signals of interest (e.g., variability patterns) are often embedded in noisy, high-dimensional measurements. As illustrated in Figure 4, a typical autoencoder is composed of three main components: an encoder, a latent embedding (or bottleneck layer), and a decoder. The encoder is often implemented using CNNs, which are well-suited for learning spatial and frequency-

¹¹ <https://lightkurve.github.io/lightkurve/>

¹² <https://scipy.org/>

¹³ <https://pytorch.org/>

¹⁴ https://github.com/waleey/ae_classifier.git

localized features (Y. LeCun et al. 1998). It transforms the high-dimensional input data into a compact latent representation that preserves the most salient features. This intermediate representation is referred to as the embedding or latent space. The decoder, typically a mirror reflection of the encoder in structure, performs the inverse operation—reconstructing the original input from the embedding using a sequence of transposed convolutions and upsampling layers. The training objective of an autoencoder is to minimize the reconstruction error between the original input and the output produced by the decoder, typically using mean squared error (MSE) or other suitable loss functions. By optimizing this reconstruction loss, the network learns to capture the essential structure of the data while discarding irrelevant variations such as noise.

In this work, we employed a convolutional autoencoder to learn a low-dimensional representation of periodogram signals associated with various stellar variability classes. These embeddings encapsulate key frequency-domain features characteristic of each variability type (e.g., solar-like oscillators, other pulsators, eclipsing binaries, rotational variables, and non-variables), providing a compressed but informative summary of the periodogram (See Section 7.3 for more discussion). Once trained, these embeddings serve as input features to a downstream classification network, which assigns labels to different variability types based on their learned frequency domain structures. A simple representation of the network is in Figure 4, and a more detailed structure can be found in Section 7.2.

The autoencoder design used in this study was mainly inspired by the work of B. J. Ricketts et al. (2023), who developed an algorithm for mapping the X-ray variability of black hole binaries. This neural network was comprised of two main sections: encoder and decoder. Both sections had 9 convolutional layers in conjunction with pooling and dense layers to reduce the input dataset to lower dimension.

We applied significant changes to the autoencoder to make it suitable for our case. We made the network deeper by adding 5 more convolutional layers in both encoder and decoder. This structure was chosen because of the large dimensionality of our input signal (4096) compared to smaller input dimension (256) of B. J. Ricketts et al. (2023). Moreover, each convolutional block includes a `BatchNormalization` layer, which normalizes the output of the preceding layer to stabilize and accelerate training by improving gradient flow. For the convolutional and dense layers, we used `kaimin_normal` (K. He et al. 2015) weight initialization, and for `BatchNorm1d` layers, we used constant weight ini-

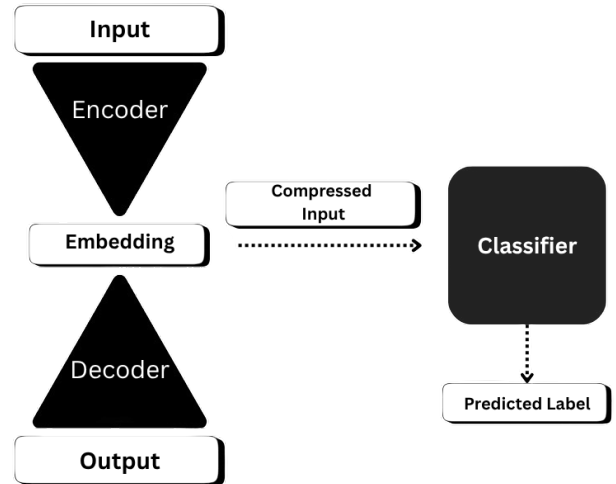


Figure 4. Schematic diagram of the autoencoder and classifier developed for this study.

tialization technique. We also employed a `leaky_relu` activation function to mitigate the vanishing gradient problem and ensure better feature propagation, particularly for large and diverse datasets. In addition, a `Dropout` layer with a probability of 0.4 is incorporated to reduce overfitting by preventing the network from relying too heavily on specific neurons and promoting more robust generalization.

To facilitate learning of both local and global frequency domain features in the periodogram signals, we adopted a varying set of kernel sizes in the convolution layers of encoder and decoder. A kernel size specifies how many neighboring data points a convolutional filter spans, determining the local region over which it extracts features. Smaller kernels (e.g., size 1 and 3) are well-suited to learn fine-grained, local features such as sharp peaks due to a rotation signals or oscillation power excess envelopes in solar-like oscillators (K. Simonyan & A. Zisserman 2015). Large kernels (e.g., 7, 11, 15) allow the network to learn more extended patterns and global structures which was key in distinguishing the granulation background from other types of noise (F. Yu & V. Koltun 2016).

To facilitate dimensionality reduction, we have experimented with (1) strided convolution¹⁵ and (2) `MaxPooling`¹⁶. The strided convolution technique generated artifacts in the reconstructed signal (see e.g. Y. Kinoshita & H. Kiya 2020 for a similar discussion) and

¹⁵ <https://www.deeplearningbook.org/contents/convnets.html>

¹⁶ <https://pytorch.org/docs/torch.nn.MaxPool1d.html>

was unable to reconstruct the fast-varying features in the periodogram. `MaxPooling`, on the other hand, could accurately reconstruct those fast variations without producing any artifacts. Therefore, we decided to continue using `MaxPooling` as our dimensionality reduction technique.

The latent space dimension of 128 was chosen by means of trial and error. Initially, we started with a latent space dimension of 32, which yielded a classification accuracy of 87% for solar-like oscillators. Then, we moved up to a 64-dimensional latent space, which resulted in a classification accuracy of 97% for solar-like oscillators, but only 77% classification accuracy for identifying stars that do not show solar-like oscillation, referred to as `NonSOLR` in this text. To investigate the low classification accuracy, we analyzed the reconstructed periodograms and found that although these low-dimensional latent spaces were able to capture the slowly varying granulation background, they were consistently missing the oscillation hump, which shows up as Gaussian envelopes. Finally, in a 128-dimensional latent space, we reached appreciable accuracy in the classification of both solar-like oscillators and other types of variables, and visual inspection of the reconstructed periodograms also revealed that the model improved at capturing those oscillation humps it was missing in a lower-dimensional latent space. We also tried making the latent space size 256-dimensional, and the accuracy of finding solar-like oscillators increased to 99.7%, but the accuracy for finding other types of variables increased to 95%. Although it reduced the number of false positives by 0.8%, this larger latent space also increased the convergence time for training the model by about 30 minutes and required increased memory for storing the latent space representation of the input signal. Therefore, we decided to continue our analysis with a 128-dimensional representation.

For upsampling in the decoder, we used the cubic interpolation function provided by `PyTorch`¹⁷. We also explored other techniques such as strided convolution and `MaxUnpooling`, but both techniques generated artifacts in the reconstructed periodograms and gave higher reconstruction loss compared to the cubic interpolation approach. Therefore, we did not consider those techniques in our study. Also, to enhance the model’s ability to focus on the region of the periodograms with the most information, we used attention layers which dynamically weights the importance of different input positions, allowing the model to focus on the most relevant parts of

the sequence when making predictions. Attention layers are known for its ability to selectively amplifying important features and suppress noise (A. Vaswani et al. 2017).

To quantify our error in the reconstructed signal compared to the original input in autoencoder, we used the mean squared error (MSE) loss function. A minimal reconstruction loss signifies the decoder is able to successfully reconstruct the original input from the embedding layer, which in turn means the embedding contains the most important information about the variability patterns of the periodograms. We also tested the Mean Absolute Error (MAE) loss function, but did not see any noticeable improvement in the performance of the network and it was not considered further.

3.2. Classifier

We classified the compressed representation of the input signal from the autoencoder in one of two categories: `SOLR` and `NonSOLR`. In order to handle classification tasks, the autoencoder has a classifier head attached to the embedding layer (See Figure 4). Therefore, the autoencoder works as an automated feature extraction network and the classifier is an estimation network that predicts the labels based on those extracted features. Our classifier is a standard `mlp` network (D. E. Rumelhart et al. 1986) with two dense layers, one activation function and a dropout layer. This composite architecture of combining autoencoder with a classifier is inspired by the work of S. Jamal & J. S. Bloom (2020). The first dense layer has an input length of 128. This layer outputs a sequence of 16 points that the second dense layer encodes into one output number. During training and validation, the raw output value is passed on to the loss function to calculate the classification loss. Since we are doing a binary classification task, we have used `BCEWithLogits()` as our classifier loss function. `BCEWithLogits()` is given by the following equation:

$$\mathcal{L}_C = \frac{1}{N} \sum_{i=1}^N w_{y_i} \left[-y_i \cdot \log(\sigma(\hat{z}_i)) - (1 - y_i) \cdot \log(1 - \sigma(\hat{z}_i)) \right] \quad (1)$$

where,

$$\sigma(\hat{z}_i) = \frac{1}{1 + e^{-\hat{z}_i}} \quad (2)$$

where \hat{z}_i is the raw logit output from the model for i -th sample, $y_i \in \{0, 1\}$ is the provided true label for the same sample, and N is the number of signals in the batch. Also, w_{y_i} is an extra weight factor multiplied to

¹⁷ <https://pytorch.org/>

each element of a sample that depends on the sample’s class. Thus for a given sample from a given class, each element has the same weight factor. This forces the loss function to put equal emphasis on the minority class (in our case SOLR) as the majority class (NonSOLR, see Table 1). To see the detailed architecture of the classifier network, please refer to S. Jamal & J. S. Bloom (2020).

3.3. Training, Validation & Testing

We split the dataset using a 80–20 train-test split using a random number generator, which resulted in 92,896 objects in the training sample, and 23,224 signals in the test sample. This splitting was done based on unique TIC IDs because SOLR sample has signals from multiple sectors, and the same star being in both the training, validation, or test set will cause contamination between the sets, preventing correct generalization of the underlying signals. Finally, the training sample was further split into 70–30 training-validation set, resulting in 65,027 stars in the final training set and 27,868 stars in the validation set, using unique TIC IDs as discussed above. The training and validation set was used during the training phase of the NN, and the test set was kept hidden and only used to calculate prediction accuracy of the model.

We experimented with two different training schemes: sequential training and joint training. In sequential training, we trained only the autoencoder first by minimizing reconstruction loss given by MSE loss (see Section 3.1) and then trained the classifier to minimize classification loss given by Equation 1. This gave the best performance for the neural network in predicting the labels in the test set, since the autoencoder worked as a stand alone feature extraction algorithm that contained the most important spatial features of the periodograms in the embedding space, and the classifier worked as an independent estimation network to predict the labels based on extracted features. We also tried training the network in the joint scheme where we trained both autoencoder and classifier simultaneously, and tried to minimize total loss given by the direct sum of MSE and classifier loss (Equation 1). However, this produced poor reconstruction, resulting in almost 10 times higher reconstruction loss compared to sequential training (see Figure 5). One possible strategy to mitigate this issue during joint training is to apply a time-dependent weighting scheme to the two loss components, such that the reconstruction loss dominates the early stages of training. This allows the autoencoder to first learn the salient features of the input representation, after which the weights can be gradually balanced between the reconstruction and classification losses to improve classi-

Table 2. Hyperparameters used for training.

Hyperparameter	Value
AE Learning Rate	1×10^{-3}
Classifier Learning Rate	1×10^{-4}
Batch Size	64
Embedding Size	128
min_delta	1×10^{-4}
patience	50

fication performance. However, because the sequential training scheme already yielded robust and satisfactory results without the need for additional complexity, we adopt this approach for the present study.

The probability that a given star exhibits solar-like oscillations was obtained by applying a `softmax()` activation function to the classifier output. This operation maps the raw network logits to normalized probabilities in the range $[0,1]$, where values closer to 1 indicate a higher likelihood of the star being a solar-like oscillator. For the computation of validation accuracy, we adopted a classification threshold of 0.5: stars with softmax probabilities greater than this threshold were labeled as SOLR, while those below were labeled as NonSOLR.

Our training procedure follows a standard neural-network optimization workflow, using gradient-based updates and empirically tuned hyperparameters. The neural network uses a gradient descent algorithm that updates the parameters to minimize loss function. For gradient descent, we have used Adam Optimizer (D. P. Kingma & J. Ba 2014) with learning rates 1×10^{-3} for autoencoder training and 1×10^{-4} for classifier training. Since using a fixed learning rate provided satisfactory results, we did not use any learning rate scheduler. All hyperparameters including learning rate, batch size, size of the embedding layer were selected by trial and error and can be found in Table 2. We also implemented an early stopping procedure based on the validation loss, meaning that training was halted when the validation loss failed to improve for a fixed number of epochs (patience), in order to prevent overfitting and ensure the model retained good generalization performance. The min_delta and patience parameters for early stopping is also found based on trial and error and listed in Table 2. We also trained our network on Google Colab¹⁸ T4 GPUs. The autoencoder training took 4 hour 24

¹⁸ <https://colab.research.google.com/>

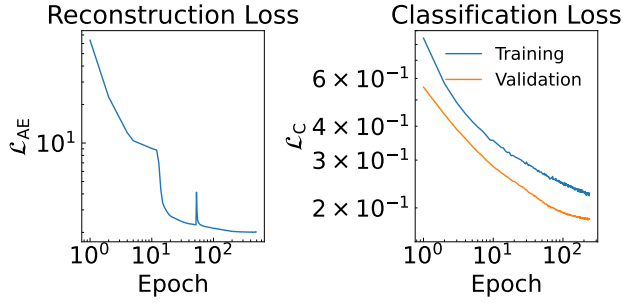


Figure 5. Loss as a function of epochs for autoencoder (left) and classifier (right). Only training loss is shown for autoencoder while both training and validation loss is shown for classifier. We computed validation loss for all epochs only for the classifier network.

minutes and the classifier training took around 2 hour 11 minutes.

Figure 5 displays the reconstruction and classification losses for the autoencoder and classifier, respectively. During the initial autoencoder training phase, we only record the training reconstruction loss, as validation is not performed until the autoencoder training concludes, given that the validation set is not used during autoencoder training. Instead, we monitor the training loss and apply early stopping once it plateaus. At that point, we freeze the autoencoder weights, and begin training the classifier on top of the learned representation. Since we are not training the autoencoder anymore, we only compute the validation loss for it, and the loss stayed stable at a value of 2.14, which is extremely close to its training loss before freezing.

In the classification loss, shown in the right panel of Figure 5, we observed that the validation classification loss was slightly lower than the training loss. This is due to the use of dropout layers during training, which randomly deactivates neurons, effectively reducing model capacity. In contrast, dropout is disabled during validation, allowing the model to utilize its full capacity, which can result in slightly better performance. However, the difference between training and validation classification loss is minor and diminishes with more training epochs, suggesting it does not significantly affect model performance. We confirmed this by lowering the dropout probability, which reduced the gap between training and validation losses. Despite the small discrepancy, we retained the dropout layers to promote better generalization, as it improved our validation loss.

We trained the model till the early stopping procedure kicked in, as discussed above, and saved our trained model. Then, we used this model to calculate the classification metrics and confusion matrix on our test set that was hidden from the model during training phase. We

Table 3. Validation metrics and their definitions.

Metric	Definition	Value
Precision	$\frac{TP}{TP + FP}$	0.945
Recall	$\frac{TP}{TP + FN}$	0.998
F1 Score	$2 \cdot \frac{Precision \cdot Recall}{Precision + Recall}$	0.971

NOTE—Accuracy metrics and their corresponding definitions. TP, FP, FN, and TN denote true positives, false positives, false negatives, and true negatives, respectively. All metrics are calculated on an independent test set.

evaluated the model performance using three standard classification metrics: precision, recall, and F1 score. Precision is defined as the fraction of predicted positive samples that are truly positive, and thus quantifies the model’s ability to avoid false positives. Recall is defined as the fraction of actual positive samples that are correctly identified, minimizing false negatives: an important consideration in our application where missing positive detections is particularly undesirable. The F1 score represents the harmonic mean of precision and recall, providing a balanced measure of both metrics. The formal definitions and corresponding values of these metrics for the validation dataset are summarized in Table 3. Our precision is 0.945, meaning the model is able to avoid false positives with probability 0.945. A recall of 0.998 signifies the fraction of actually positive samples recovered during validation. Our F1 score is 0.971, meaning our model has high accuracy in recovering the true samples, as well as robust against negative samples.

As a final test of our model we estimated the values of the confusion matrix, which is shown in Figure 6. The model achieved 99.8% accuracy in recovering the solar-like oscillators (SOLR) and 94.2% accuracy for stars that do not have solar-like oscillation (NonSOLR). 5.8% of the NonSOLR were misclassified as SOLR, and most of these false positives are non-variables. Upon investigating the periodogram of these non-variables, we found that they have a low-frequency granulation like slope in their periodogram, which likely made the network classify them as solar-like oscillator. On the other hand, 0.2% of the SOLR type stars were misclassified as NonSOLR. These stars have a median ν_{\max} of 300 μHz . After investigat-

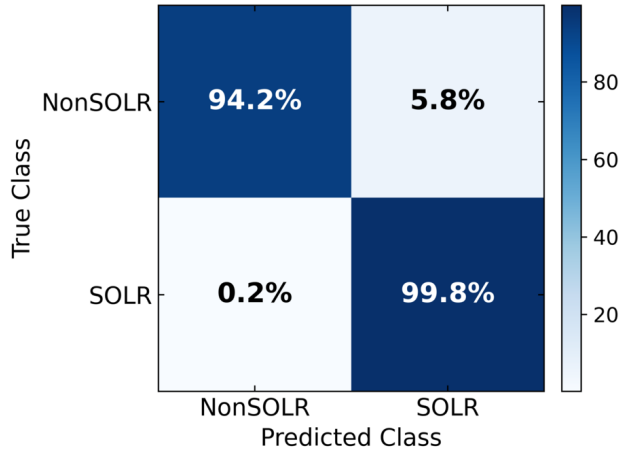


Figure 6. Confusion Matrix for test set. Here, SOLR refers to solar-like oscillator and NonSOLR refers to stars that do not exhibit solar-like oscillation. The color bar describes the fractional percentage in each panel between 0 and 1. True positive is 99.8% and true negative is 94.2%. False positive and false negative are 5.8% and 0.2% respectively.

ing their periodograms, we found that for most stars, the low-frequency correlated noise and the granulation signal overlap with the oscillation signal, which makes it harder for the neural network to distinguish them. However, since we are interested in stars with comparatively higher frequency, this is within our acceptable margin of error.

4. FINDING NEW PULSATION SIGNALS

In this section, we outline the methodology employed to identify new solar-like oscillator candidates. We begin by describing the target sample used for the search, which was analyzed using the neural network architecture detailed in Section 3. We then present the newly identified candidates and characterize their properties. Most of our analysis was done on 2 min cadence data as discussed before, and we complemented this analysis with 20-sec data discussed in Section 4.3. Finally, we added a comparison with previously reported solar-like oscillators.

4.1. Target Selection

Our target sample was selected from the TESS asteroseismic target list (ATL, T. L. Campante 2017; M. Schofield et al. 2019), a list of asteroseismic targets compiled before the launch of TESS to streamline its target selection process for 2 min cadence. The authors of the ATL used fundamental stellar parameters and scaling relations to predict oscillation frequencies (ν_{\max}) and amplitudes of solar-like oscillations. Combining these values with the photometric noise characteristic

of TESS, they calculated a detection probability following the method described in W. J. Chaplin et al. (2011). For our analysis, we used a revised version of the ATL (D. Hey et al. 2024) that used an updated ν_{\max} scaling relation considering surface gravity data available from *Gaia* DR3 (Gaia Collaboration et al. 2016, 2023), and an updated amplitude scaling relation derived from Kepler observations (D. Huber et al. 2011).

After cross-matching the entire ATL sample with *Gaia* stellar parameters based on *Gaia* ID, we selected stars with a $(G_{\text{BP}} - G_{\text{RP}}) \geq 0.78$, which corresponds approximately to stars colder than G0 dwarfs ($T_{\text{eff}} \leq 5930$ K)¹⁹ (M. J. Pecaut & E. E. Mamajek 2013). We kept only stars in the main sequence and sub-giant branch, based on their position in the *Gaia* color-magnitude diagram (CMD). We also applied a frequency cut based on the ATL predicted ν_{\max} and selected stars with $\nu_{\max} \leq 4167 \mu\text{Hz}$, to remove stars with predicted frequency faster than the TESS 2 min cadence Nyquist limit of $4167 \mu\text{Hz}$. We downloaded the SPOC light curves for the remaining 81,642 stars using their TIC IDs, and we pre-processed the signals in the same manner described in Section 2. We also removed the known solar-like oscillators that were used to train, validate, and test our model as described in Section 3. Our final sample included periodograms of 81,642 stars, which were then passed on to the neural network, described in Section 3, to estimate their probability of having solar-like oscillations.

For each target, the neural network outputs a probability of having solar-like oscillations between 0 and 1. From this output, we found that the majority of high-probability targets are clustered near the sub-giant branch, and the probability gradually decreases towards the low-temperature region along the main-sequence.

To remove targets that are unlikely to show solar-like oscillations, we selected stars with probability ≥ 0.5 (this cut was also used during training process), yielding a sample of 3463 candidates. This list of candidates can be found in Table 4.

4.2. Vetting of Candidates

In this section, we describe the manual vetting process of the shortlisted target sample produced by the neural network. For the vetting process, we leveraged the known properties of solar-like oscillators and pySYD (A. Chontos et al. 2022), an open source Python package to automatically calculate global oscillation parameters, to further shortlist our candidate list. A step-by-step description of this process is given below.

¹⁹ <https://www.pas.rochester.edu/~mamajek/>

Table 4. Asteroseismic and stellar parameters of all candidates with Probability ≥ 0.5 of being a solar-like oscillator as determined by neural network algorithm.

TIC	R_*	T_{eff}	ν_{max} (Predicted)	SNR	Probability	Candidate
	$[R_{\odot}]$	[K]	$[\mu\text{Hz}]$			
34860555	1.264	6095	1323.83	0.621	0.76	0
8193616	1.249	5629	1896.17	1.094	0.59	0
6528048	1.418	5877	1818.08	1.322	0.67	0
4995808	1.830	5382	1065.62	3.664	0.55	1
9333731	1.892	5904	826.96	4.149	0.64	1

NOTE—Columns are: TESS Input Catalog identifier (TIC), stellar radius R_* , effective temperature T_{eff} , frequency of maximum power ν_{max} , signal-to-noise ratio (SNR), and Probability of exhibiting solar-like oscillation as determined by the neural network (Probability). Finally, the Candidate columns denote whether the star is included in our candidate sample in Section 4. A full version of this table containing all 3463 candidates with probability ≥ 0.5 can be found online.

Solar-like oscillations are characterized by a Gaussian-like power excess envelope near the frequency of maximum power (ν_{max}). Moreover, they have evenly spaced radial overtones for a fixed angular degree of oscillation mode. This results in evenly spaced peaks near ν_{max} in their periodogram. This feature can be revealed by calculating auto-correlation functions (acf) of their background-corrected periodogram and identifying periodic patterns. Moreover, this also means their échelle diagram will have vertical ridges for the right choice of large frequency separation ($\Delta\nu$). To identify these properties, we calculated the background-corrected power spectrum, ν_{max} and acf using `pySYD`. Furthermore, we calculated their échelle diagram using the `echelle` package (D. Hey & W. Ball 2020).

In the subsequent stage of our analysis, we applied a series of selection criteria to refine the candidate list: (1) We required consistency between the ν_{max} values derived using `pySYD` and those predicted in the ATL catalog. The `pySYD` algorithm models the oscillation power excess as a Gaussian envelope characterized by a central frequency and width (1σ); candidates were retained if the ATL-predicted ν_{max} lay within this envelope; (2) We required the presence of periodicity in the acf; (3) We excluded targets affected by background contamination by conducting a 15–20 arcmin search around each star and comparing the light curves of nearby sources to identify potential blending or flux leakage; (4) Finally, we visually inspected the échelle diagrams and retained only those stars exhibiting well-defined, vertically aligned ridges indicative of regular frequency spacing. In this process, we also removed the stars that were previously identified as solar-like oscillators and were not part of our training process (see Section 4.4).

Figure 7 shows five examples of our manual vetting process and includes the full power spectra, background-corrected power spectra, autocorrelation functions, and échelle diagrams for five main sequence G and K dwarf candidates indicated on the radius-temperature plot (Figure 8). The first column contains the power spectrum, where the expected ν_{max} from ATL catalog is represented by a dotted red line. The observed ν_{max} calculated using the `pySYD` package and the width of the gaussian envelope around it is shaded in gray. The second column contains the background-corrected power spectrum zoomed in near the observed ν_{max} , followed by autocorrelation function in third column, and échelle diagram in the fourth.

All five candidates in Figure 7 have periodic auto-correlation function, and their échelle diagrams show dark vertical ridges. The predicted ν_{max} for all five candidates, denoted by the dotted red line, agrees with the observed ν_{max} using `pySYD`. Diagnostic plots for all the rest of the interesting candidates are provided in the Appendix 7.

This analysis greatly reduced our number of candidates. Out of the 3463 stars, 23 stars satisfied all four criteria, with a few exceptions that we discuss later in this section. We did not exclude any candidates based on signal-to-noise ratio. This choice was made given that previous works have shown that for faint stars with low signal-to-noise ratio, oscillation features, such as $\Delta\nu$, can be revealed by a periodic acf, even when a reliable measurement of ν_{max} is not possible (e.g., M. Sayeed et al. 2025; W. J. Chaplin et al. 2014b). Table 5 contains the asteroseismic parameters ν_{max} and $\Delta\nu$ derived in this study along with fundamental stellar parameters of these 23 stars. This table also includes one candidate found using TESS 20 second search discussed in Sec-

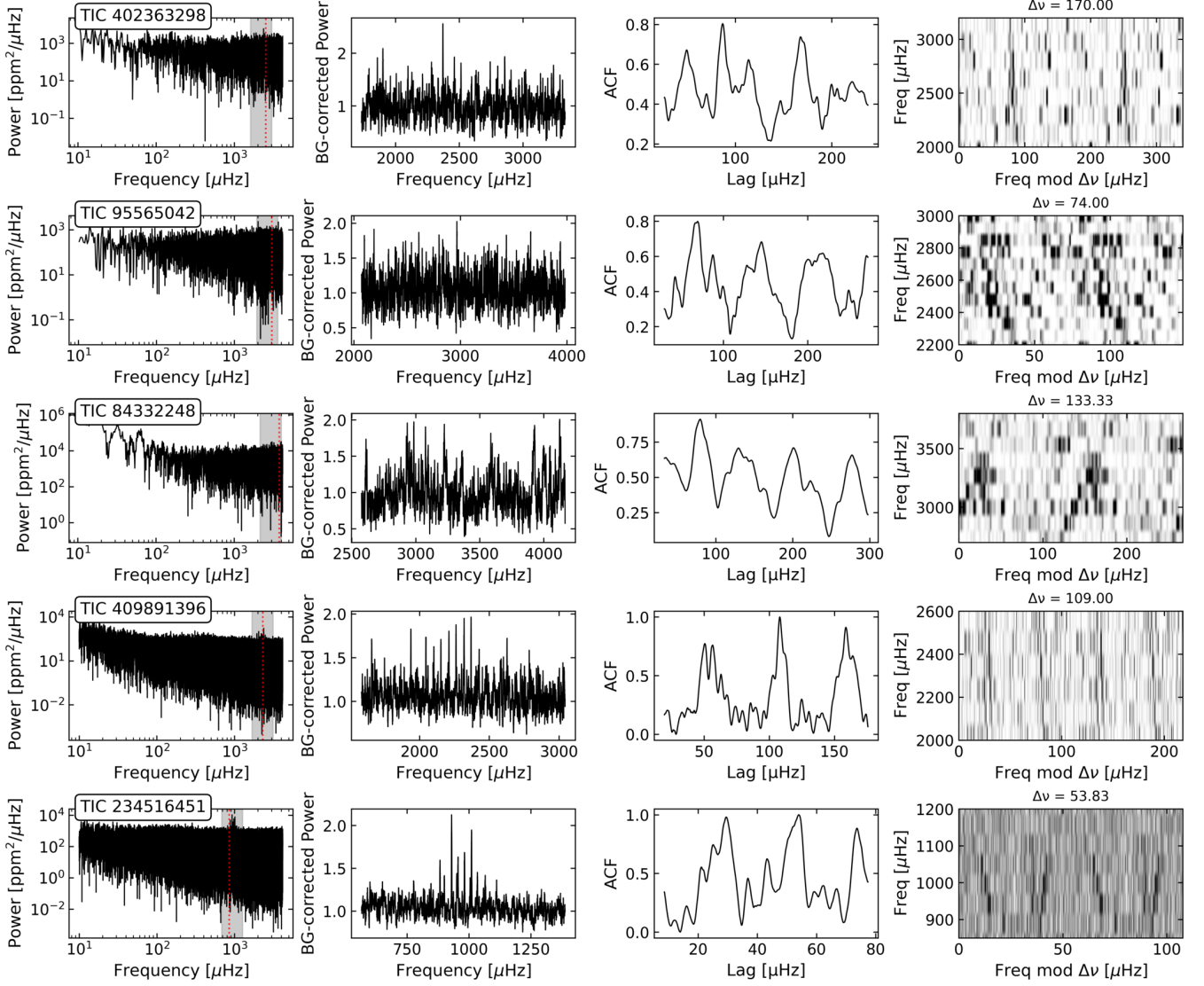


Figure 7. Diagnostic plots for five solar-like oscillator candidates from Figure 8 with TIC 402363298, 95565042, 84332248, 409891396, and 234516451 respectively. *First Column:* power spectrum with region near observed ν_{\max} is shaded in dark grey and predicted ν_{\max} from scaling relation in dotted red line, *Second Column:* background-corrected power spectrum zoomed-in on expected ν_{\max} , *Third Column:* auto-correlation function, *Fourth Column:* échelle diagram. TIC 402363298 and 84332248 are in K dwarf region, TIC 95565042, 409891396, and 234516451 in G dwarf region.

tion 4.3. To calculate the signal-to-noise ratio (SNR), we used running median of the periodogram as the noise level. In cases where the periodogram has a clear power excess, height of that peak was used as signal, otherwise height of the maximum peak near the region of expected ν_{\max} was chosen to be the signal. The stellar parameters T_{eff} and radius were taken from Gaia DR3 (Gaia Collaboration et al. 2023) and Tess Input Catalog (K. G. Stassun et al. 2018).

A radius-temperature plot of our 23 candidates is shown in Figure 8 against previously discovered solar-like oscillators using photometry from TESS and Kepler, and radial velocity measurements. The solar-like

oscillators from Kepler were taken from S. Mathur et al. (2017), which provided a catalog of 12,777 solar-like oscillator. The TESS discoveries of this figure are from E. Hatt et al. (2023), as described in Section 2, that added 4177 solar-like oscillator across main-sequence, sub-giant and giant branch in H-R diagram. The 12 radial velocity candidates are taken from T. Arentoft et al. (2008), H. Kjeldsen et al. (2008) and references therein. The plot also includes our candidates that were found using 20 second cadence only, which will be discussed in Section 4.3.

Our stars are color-coded by their signal-to-noise ratio. As expected, the majority of candidates lie in

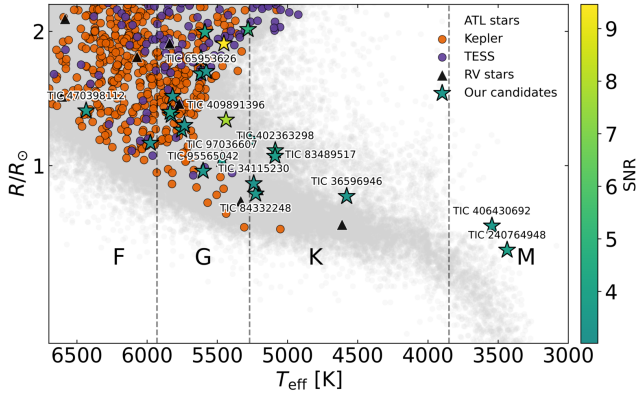


Figure 8. Stellar radius versus effective temperature plot for our candidates (star symbol) and previously discovered solar-like oscillators using TESS (violet circles), Kepler (orange circles), and radial velocity (black triangles). Our candidates are color-coded by their signal-to-noise ratio. TESS and Kepler stars were taken from E. Hatt et al. (2023) and S. Mathur et al. (2017), respectively. Radial velocity candidates were obtained from T. Arentoft et al. (2008), H. Kjeldsen et al. (2008) and references therein. Every star with TIC ID in the figure is discussed in Section 5. Stars without TIC IDs are more common targets, which are also discussed in Section 5. These candidates satisfy the following conditions: (1) existence of power excess near predicted ν_{\max} , (2) contains periodic auto-correlation function (3) no contamination from stars in the background, and (4) existence of vertical ridges in échelle diagram.

the G-dwarf regime, with effective temperatures in the range $5270 K \leq T_{\text{eff}} \leq 5930 K$, consistent with most previous TESS detections. The impact of our work is most evident at cooler temperatures, particularly for $T_{\text{eff}} \leq 5000 K$, where no solar-like oscillators had previously been identified using TESS. In this regime, we identify two main-sequence candidates (TIC 36596946 and TIC 418544237), as well as two cooler candidates located above the main sequence with $T_{\text{eff}} \leq 3800 K$ (TIC 406430692 and TIC 240764948). From left to right in the figure, the signal-to-noise ratio decreases systematically, as expected, reflecting the lower oscillation amplitudes of cooler stars.

4.3. 20 Second Search

Following our analysis of TESS 2 min cadence light curves using the neural network and pySYD, we additionally examined the available 20 second cadence light curves from TESS for the targets of the ATL catalog (D. Hey et al. 2024). From the ATL target sample described in Section 4.1, 13,620 stars had 20 second cadence light curves in TESS. We first binned the light curves of these stars to 2 min cadence to make them compatible for our analysis using the neural network described in Section 3. After analyzing their signals using the neural network in

the similar manner as their 2 min counterpart, 596 stars had a probability > 0.5 of having solar-like oscillation. Then we manually vetted the candidates using pySYD and echelle package using the criteria outlined in Section 4.2. This process yielded four stars, three of which (TIC 65953626, TIC 409891396, and TIC 234516451) were already present in our candidate list based on the 2 min cadence analysis. These three candidates were also the only 2 min candidates that also had 20 second cadence, so this analysis strengthens their candidacy and does not discard any other 2 min candidates from Section 4.2. The only new candidate from the 20 second cadence data is TIC 97036607. This new candidate is included in our radius-temperature plot in Figure 8 and in our candidate list in Table 5.

Diagnostic plots for TIC 65953626, TIC 409891396, and TIC 234516451, using the 20 second data, are shown in Figure 9. As evident from these plots, the SNR of the first two candidates improved substantially to 4.029 and 9.089, respectively, compared to the values reported in Table 5, whereas the SNR of the last candidate decreased to 7.41303. In addition, the auto-correlation functions exhibit a more pronounced periodic structure, and the ridges in the échelle diagrams are more clearly defined. For TIC 409891396 in particular, the background-corrected power spectrum reveals a greater number of radial overtones relative to the 2 min cadence results shown in Figure 7. These improvements provide strong support for the robustness of the candidate list presented in Figure 8. With the availability of 20 second cadence data for all candidates, the detection of solar-like oscillations in these stars can be further strengthened and, in some cases, confidently confirmed.

TIC 97036607 is a main-sequence late G dwarf which has a low SNR (3.49), and its power spectrum does not have any visible power excess. However, the existence of periodic structures in the autocorrelation function and evidence of two dark ridges in échelle diagram make it a compelling candidate. We also investigated the 2 min cadence data of this star, and found that although it was classified as solar-like oscillator by the neural network, its autocorrelation function did not show such periodic pattern and we did not find any ridges in its échelle diagram. Only in 20 second cadence data was the oscillation signal strong enough to show these diagnostic features. A summary plot of these diagnostic features can be found in Figure 10.

4.4. Comparison to Previous Detections

In this section, we discuss the general overlap between the ATL catalog and previously detected solar-like oscillators using Kepler and radial velocity techniques. Then

Table 5. Asteroseismic and stellar parameters of candidate stars exhibiting periodic auto-correlation functions and dark vertical ridges in their échelle diagrams.

TIC	R_*	T_{eff}	ν_{max}	$\Delta\nu$	PE	SNR	Cadence
	$[R_{\odot}]$	[K]	$[\mu\text{Hz}]$	$[\mu\text{Hz}]$			
84332248	0.864	5226.7	3070.21	133.33	1	3.443707238	2 min
314805964	1.147	5270.8	2274.71	115.41	1	3.439693346	2 min
65953626	1.608	5616.8	1222.75	66.33	1	3.626556000	2 min + 20 sec
402363298	1.081	5086.9	2312.52	170.00	0	4.252623103	2 min
409891396	1.266	5437.5	2400.00	109.00	1	7.771395930	2 min + 20 sec
9102735	1.627	5578.6	1142.96	67.80	1	3.267807716	2 min
9333731	1.992	5588.0	733.13	43.00	1	4.149027362	2 min
330014070	1.430	5817.6	1682.50	99.00	0	3.101131390	2 min
406430692	0.733	3543.9	1700.10	131.50	0	3.470821167	2 min
211227897	1.298	5828.1	1711.02	76.00	0	3.330173687	2 min
240764948	0.647	3435.7	2166.91	105.00	1	3.894182859	2 min
34115230	0.912	5240.3	3363.51	102.00	0	3.197691186	2 min
79279141	1.318	5835.9	1848.90	64.10	1	3.923868602	2 min
20887793	1.124	5976.8	2108.20	94.50	1	3.016192161	2 min
36596946	0.854	4578.2	3325.50	137.00	1	3.380654612	2 min
4995808	1.740	5615.8	952.65	36.00	1	3.664899277	2 min
83489517	1.050	5088.5	2234.99	87.50	0	3.710662560	2 min
92254955	1.202	5753.7	2250.00	103.00	0	3.660322086	2 min
95565042	0.973	5600.7	2774.66	74.00	1	3.379471087	2 min
97917479	1.232	5733.6	1288.84	80.00	0	3.202157115	2 min
333704881	2.021	5280.5	830.00	31.50	0	4.935405533	2 min
470398112	1.328	6433.8	1850.29	72.50	1	3.636444166	2 min
234516451	1.876	5453.0	977.63	53.83	1	9.460528	2 min + 20 sec
97036607	1.0327	5467.3	2241	75	0	3.488465	20 sec

NOTE—Columns are: TESS Input Catalog identifier (TIC), stellar radius R_* , effective temperature T_{eff} , frequency of maximum power ν_{max} , large frequency separation $\Delta\nu$, presence of a visible power excess (PE; 1 = yes, 0 = no), and signal-to-noise ratio (SNR).

we point out how many of these candidates were selected in the sub-sample of ATL that we used to test the neural network and how many of them were recovered as solar-like oscillators.

Our sample was taken from the ATL catalog, which initially had 1,985,986 stars. Then, we cross-matched these stars with *Gaia*, and cleaned the sample based on $(G_{\text{BP}} - G_{\text{RP}})$ and position in the H-R diagram as described in Section 4.1. Furthermore, we also removed the stars that were already in our training set described in Section 2. This resulted in 267,849 stars, out of which only 81,642 stars had TESS light curves that we passed on to the neural network to find new solar-like oscillators. In the test sample of this 81,642 stars, 10 stars were previously identified as solar-like oscillators in the literature using Kepler and radial velocity techniques (S.

Mathur et al. 2017; T. Arentoft et al. 2008; H. Kjeldsen et al. 2008). Our neural network was able to recover 7 of these stars as solar-like oscillators, with probability greater than 0.5. We then processed these 7 stars through the pySYD pipeline, and only one of them, which was originally detected using Kepler, satisfied our four criteria laid out in Section 4 to be classified as candidate for solar-like oscillator. A summary of these 10 stars, their diagnostic properties to exhibit solar-like oscillation, and fundamental properties can be found in Table 6.

TIC 419015728 and TIC 231698181 were identified as solar-like oscillator in T. Arentoft et al. (2008) and T. L. Campante et al. (2024) using radial velocity technique, but our neural network could not recover them. Their ν_{max} is 4244.57 μHz and 4228.75 μHz respectively, which is beyond the Nyquist limit of 4167 μHz in TESS 2 min

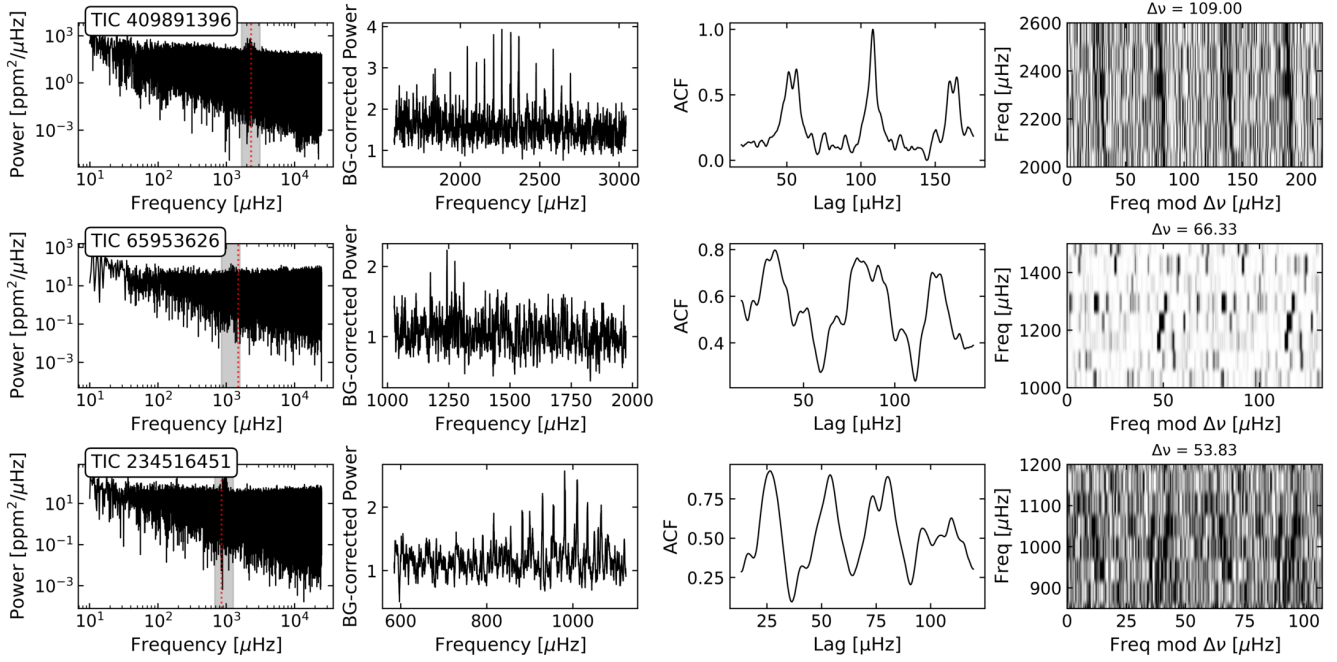


Figure 9. Diagnostic plots for two solar-like oscillator candidates from Figure 8 with TIC 65953626, and 409891396 using TESS 20 second cadence. *First Column:* power spectrum with region near observed ν_{\max} is shaded in dark grey and predicted ν_{\max} from scaling relation in dotted red line, *Second Column:* background-corrected power spectrum zoomed-in on expected ν_{\max} , *Third Column:* auto-correlation function, *Fourth Column:* échelle diagram.

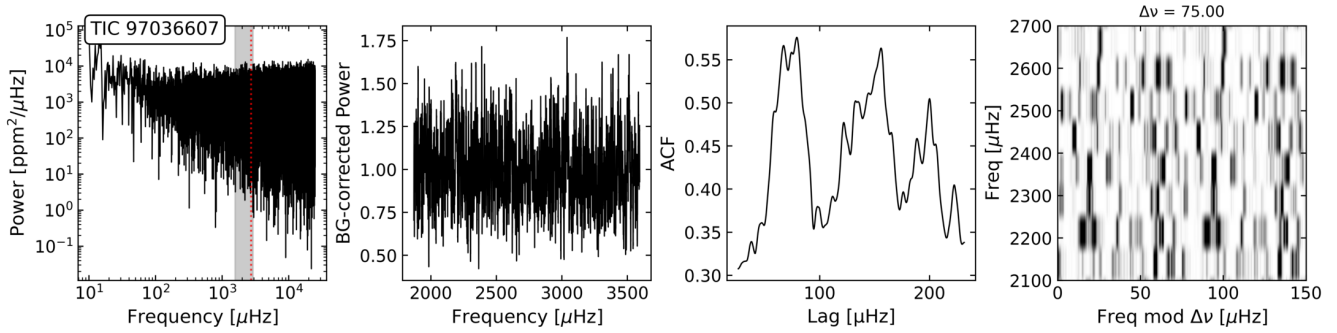


Figure 10. Same as Figure 9 for TIC 97036607.

cadence. Therefore, it is not surprising that we did not see any oscillation signal in these two stars. Both of these stars have a SNR of 2.5 (T. C. Teixeira et al. 2009; T. L. Campante et al. 2024), but the Nyquist limit of TESS 2 min cadence makes it unlikely to observe this signal. Moreover, they do not currently have 20 sec cadence in TESS, so we could not verify if the oscillation actually becomes visible in TESS.

TIC 406951876 is a K0 Giant star with temperature 5239 K. It has a ν_{\max} of 793 μHz which is well within the reach of TESS 2 min cadence. However, it was not identified by the neural network as exhibiting solar-like oscillations. From D. Hey et al. (2024), the reported oscillation amplitude using Kepler data for this star is

8.95 in arbitrary unit (a.u.), but in TESS 2 min data, the noise amplitude calculated from the median noise floor of the power spectrum has a value of 18.01 (a.u.), making it unlikely to find the oscillation signal.

Among the stars we have recovered using the neural network, only TIC 27013540 passed the four criteria we used to confirm the candidacy of solar-like oscillation mentioned in Section 4.2. This star has a ν_{\max} of 606 μHz (compared to ν_{\max} 576 μHz which we recovered), which is well within the range of TESS 2 min light curves. It also shows a periodic autocorrelation function and dark vertical ridges in its échelle diagram, which satisfies our candidacy requirements.

Table 6. List of stars in target sample that were previously identified as solar-like oscillator.

TIC	T_{eff}	ν_{max}	acf	Échelle	Recovered	Detection	Reference
	[K]	[μHz]		Diagram	NN	Method	
419015728	5333.00	4244.57	0	0	0	RV	T. Arentoft et al. (2008)
123317744	4486.75	760.68	0	0	1	Kepler	S. Mathur et al. (2017)
399952145	5284.57	4328.43	0	0	1	Kepler	S. Mathur et al. (2017)
27013540	5212.55	606.85	1	1	1	Kepler	S. Mathur et al. (2017)
394172596	5058.00	6156.30	0	0	1	Kepler	S. Mathur et al. (2017)
172424739	4289.22	3577.78	0	0	1	Kepler	S. Mathur et al. (2017)
123234496	5270.85	6035.91	0	0	1	Kepler	S. Mathur et al. (2017)
1674663309	5204.63	3046.97	0	0	1	RV	H. Kjeldsen et al. (2008)
231698181	4560.30	4228.75	0	0	0	RV	T. L. Campante et al. (2024)
406951876	5239.41	793	0	0	0	Kepler	S. Mathur et al. (2017)

NOTE— The columns are: TESS Input Catalog(TIC), effective temperature T_{eff} , frequency of maximum power ν_{max} , presence of periodic peaks in the autocorrelation function (acf), recovery of the solar-like oscillations using neural network (NN), and original detection method. The ν_{max} of the stars were obtained from the respective studies.

TIC 399952145, TIC 394172596, and TIC 231698181 have ν_{max} above the Nyquist limit of 4167 μHz for TESS 2 min cadence, which makes it very hard to observe the oscillation signal in the light curves. However, these super-Nyquist oscillation signals can reveal themselves as alias peaks in the power spectrum at a frequency lower than the Nyquist limit. This is consistent with our other observation of super-Nyquist oscillation using the neural network discussed in Section 5. Also, the neural network is trained to not only find the oscillation signal, but also the granulation background, which usually resides in the low-frequency regime of the power spectrum, enabling the neural network to identify the granulation shape.

For the remaining stars in Table 6, the values of ν_{max} lie well within the Nyquist limit of the TESS 2 min cadence, enabling the neural network to detect their variability pattern in the power spectrum created by oscillation modes. However, these stars did not satisfy the additional selection criteria outlined in Section 4.2; specifically, they exhibited neither significant periodicity in their autocorrelation functions nor the characteristic dark vertical ridges in their échelle diagrams. Nonetheless, the ability of the neural network to recover these oscillation signatures from TESS 2 min light curves, serves as a valuable validation of the model’s capacity to reliably identify subtle oscillatory features.

5. DISCUSSION OF INTERESTING OBJECTS

In the previous section we presented our solar-like oscillator candidates in both main sequence and sub-giant branch. This section includes the discussion of all the

objects that have their TIC IDs in Figure 8, which includes the most interesting objects given their low temperature. For each interesting object, we first discuss the strength of its candidacy, followed by a discussion of its fundamental stellar properties such as temperature and radius, and finally compare it with oscillators previously found in the same region of the radius-temperature plot.

TIC 240764948 is an M dwarf residing right above the main sequence in the temperature-vs-radius plot shown in Figure 8. Its power spectrum (Figure 13, row 1) does not have a visible power excess, but the predicted ν_{max} falls within the shaded area. Its autocorrelation function has repeating peaks at a frequency interval of around 50 μHz , although the shape of the peaks are not uniform across the frequency range. The strongest evidence supporting the existence of solar-like oscillations is the presence of dark vertical ridges in its échelle diagram, with one angular oscillation mode visible around $\Delta\nu \approx 95 \mu\text{Hz}$. This star has a nearby star at a distance of 4.4 arcseconds found through visual inspection. The neighbor, Gaia DR3 2596359407478746112, has a similar effective temperature (3880 K), parallax (23.80 and 23.84 mas) and proper motion ((62.16, -4.13) and (64.97, -8.62) mas/yr), making it a potential M dwarf binary system. As part of our effort to check for contamination in light curves from background stars, we used `tess_photometry` (M. Pedersen in prep) to extract the light curves of these two stars directly from their target pixel files. However, we did not find any differences between the two light curves as the stars were practically blended together. Therefore, the oscillation signal could

be coming from either of the stars. This is an interesting candidate for follow up with 20-second cadence and/or radial velocity to find oscillation, as it would be the coldest star to date with pulsation signal (see e.g. [T. L. Campante et al. \(2024\)](#) for the coldest pulsating star to date).

This candidate exhibits a larger radius and a lower ATL-predicted ν_{\max} (1827.26 μHz) than is typical for main-sequence stars of this spectral type. Given its effective temperature, it is unlikely that the star has evolved into a sub-giant. A more plausible explanation is flux contamination from a binary companion, which could bias the inferred stellar radius upward and consequently lower the predicted ν_{\max} in ATL. An alternative scenario is that the star is interacting with its companion and has become inflated, leading to an increased radius and reduced ν_{\max} . However, given their projected separation of 4.4 arcseconds, it is unlikely that the system is within the dynamical range required for such interaction. One interesting possibility in this case could be TIC 240764948 being part of an unresolved binary system, which contributed to its increase in radius calculation and lower predicted ν_{\max} . A third possibility is that the candidate is a pre-main-sequence star, which could be plausible if it were located near a star-forming region. However, using BANYAN Σ ([J. Gagné et al. 2015](#)), we have verified that this star does not lie within a young moving group.

TIC 406430692 is another M dwarf candidate that also lies slightly above the main sequence in Figure 8. It shares the same diagnostic properties as TIC 240764948. Its échelle diagram (Figure 13, row 2) has one clearly visible angular mode around 80 μHz , and there are some dark vertical patches near 20 μHz , which could be indicative of another angular mode, but we do not have enough signal strength to resolve it clearly. This star has a nearby red giant (TIC 406430687) about 65 arcseconds away. Therefore, we extracted the light curve for TIC 406430687 directly from the target pixel file by carefully selecting a mask that contains light only from this star using `tess_photometry` (M. Pedersen in prep), and re-ran our analysis using `pySYD` to see if a signal similar to TIC 406430692 appears with a larger amplitude. However, we did not find the same signal re-appearing, and concluded that TIC 406430692 does not have any contamination from the red giant.

Just like TIC 240764948, this candidate also exhibits a larger radius and a lower ATL-predicted ν_{\max} . Although it does not have a resolved equal-mass binary companion, its high RUWE value (2.9) suggests the presence of an unresolved binary system. In such a scenario, excess flux from the companion would bias the inferred

stellar radius upward and consequently lower the predicted ν_{\max} . Similar effects may also arise if the star is inflated due to tidal interaction with a close companion, as observed for TIC 406430692. Because the system is unresolved, it is difficult to conclusively rule out either of these scenarios, and further follow-up observations are required for verification. Finally, as with the previous candidate, we have verified that this star does not lie within a star-forming region.

Several of our candidates are main-sequence K dwarfs located near previously confirmed solar-like oscillators in the radius–temperature plot (Figure 8). These stars exhibit consistent asteroseismic diagnostics, including periodic peaks in their autocorrelation functions and vertical ridges in their échelle diagrams, despite differences in their predicted and observed ν_{\max} values.

TIC 84332248 and TIC 34115230 form a closely related pair of main-sequence K dwarfs. Both exhibit well-defined autocorrelation periodicity and vertical structures in their échelle diagrams, consistent with p-mode oscillations (See Figure 7, row 3 and Figure 13, row 5). TIC 84332248 shows particularly strong ridges and a measured $\Delta\nu = 133 \mu\text{Hz}$, placing it near the known oscillator 70 Oph ($\Delta\nu = 161 \mu\text{Hz}$; [F. Carrier & P. Eggenberger 2006](#)). TIC 34115230, while also located near 70 Oph in Figure 8, has a smaller spacing ($\Delta\nu = 102 \mu\text{Hz}$), consistent with its larger inferred radius. Together, these two targets probe a region of parameter space with only one Kepler detection and no prior TESS discoveries, making them especially important for follow-up.

TIC 95565042 is a G-dwarf main-sequence candidate that displays a clean, periodic autocorrelation function and a single dominant ridge in its échelle diagram, likely corresponding to a radial or dipole mode (Figure 7, row 2). Although a small number of TESS detections exist in this region of Figure 8, their density remains low, reinforcing the significance of this candidate.

A second group consists of stars that have evolved off the main sequence and lie on or near the subgiant branch. These objects generally show lower ν_{\max} values and broader mode structures but still exhibit multiple independent diagnostics consistent with solar-like oscillations.

TIC 36596946 lies close to ϵ Ind in the radius–temperature plane but has evolved slightly, resulting in a lower predicted ν_{\max} of 3663 μHz . Its observed power excess near 3300 μHz , combined with periodic autocorrelation peaks and weak but discernible échelle ridges with $\Delta\nu$ in the 20–30 μHz range (Figure 13, row 3), makes it a strong oscillation candidate. Confirming oscillations in this star would extend TESS detections

into a region of the color–magnitude diagram with no previous asteroseismic identifications.

TIC 83489517 and TIC 402363298 occupy a similar location slightly above the main sequence and share broadly comparable diagnostic behavior. Both show agreement between ATL-predicted and pySYD-derived ν_{\max} values, visible power excess near 2400 μHz , periodic autocorrelation functions, and vertical ridges in their échelle diagrams indicative of low-degree modes (Figure 13, row 4, and Figure 7, row 1). TIC 83489517 exhibits a particularly clear ridge near $\Delta\nu \approx 40 \mu\text{Hz}$, with tentative evidence for an additional mode at higher spacing, while TIC 402363298 shows ridges near 100 μHz . The difference in inferred mode spacing, despite their proximity in the color–magnitude diagram, is likely driven by low signal-to-noise limitations that affect overtone identification (e.g., W. J. Chaplin et al. 2014b).

TIC 470398112 is the hottest star in our sample, an F-type dwarf with $T_{\text{eff}} = 6433 \text{ K}$. Its diagnostic plots show a strong power excess near the predicted ν_{\max} , a periodic autocorrelation function, and prominent échelle ridges (Appendix 7, Figure 16, row 3). The unusually pronounced oscillation power, relative to cooler targets, highlights the robustness of the neural network in identifying solar-like oscillations across a wide range of stellar temperatures and evolutionary states.

The rest of the targets in Figure 8 are in the G dwarf regime, where the density of previous TESS and Kepler discovery of solar-like oscillator is the highest. Their diagnostic plots are included in Appendix 7. These stars satisfy the criteria to exhibit solar-like oscillation as discussed in Section 4.2. They have periodic peaks in their autocorrelation functions with varying degrees of periodicity. TIC 409891396 and 333704881, for example, have clear periodic structure, while TIC 249763443 has periodic peaks, but the shape of the peaks are not strictly periodic, and varies from peak to peak. However, all these candidates have dark vertical ridges in their échelle diagram. TIC 249763443 and TIC 85435539 show signs of existence of multiple angular degree in their échelle diagram with the presence of double vertical ridges. The échelle diagram of TIC 187316023 shows existence of ridges that are stretched slightly towards the right, which could be result from stellar activity (E. J. Hatt et al. 2024).

A comparison between the ATL predicted ν_{\max} and the observed ν_{\max} values measured using pySYD for all our candidates is shown in Figure 11. The stars are color-coded according to their effective temperatures. In general, we find good agreement between the two frequencies with a mean difference of 124.12 μHz . However, for stars with higher frequencies, specially for

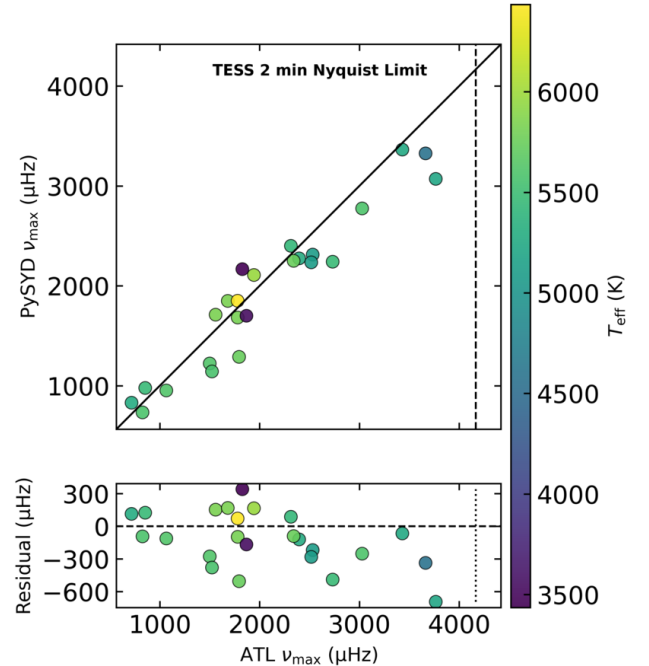


Figure 11. Comparison of predicted ν_{\max} from ATL catalog (D. Hey et al. 2024) and observed ν_{\max} using pySYD. The stars are color-coded based on their effective temperature. All the candidates with their TIC IDs are discussed in this section.

$\nu_{\max} > 3600 \mu\text{Hz}$, the difference grows larger. This frequency range lies near the Nyquist limit for TESS 2 min cadence data (4167 μHz , shown in a vertical black dashed line), suggesting that the temporal resolution of these light curves may be insufficient for reliable ν_{\max} measurements in this regime. Moreover, if the true ν_{\max} of the star is over the Nyquist limit for TESS, we might only be able to observe an alias of that signal at a lower frequency range (W. J. Chaplin et al. 2014a), which could be the case for the two candidates close to the Nyquist limit of TESS where we underpredict their ν_{\max} using pySYD.

Figure 12 contains the color-magnitude diagram (CMD) of the candidate stars color coded by their stellar mass derived using our observed ν_{\max} . We have obtained the radius and temperature of each candidate from the ATL catalog (D. Hey et al. 2024), and scaling relations from S. Hekker (2019). We have refrained from using our derived value of $\Delta\nu$ because low signal-to-noise ratio especially for late K dwarfs and early M dwarfs have prevented a reliable measurements of large frequency separation, which is consistent with previous studies (M. Sayeed et al. 2025). Without knowing $\Delta\nu$, we can only derive one of the three fundamental stellar parameters: mass, radius, and temperature, and have to use previously determined values for the other

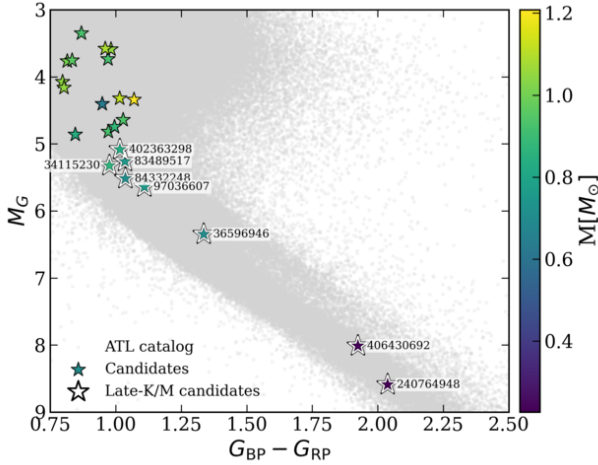


Figure 12. Color-Magnitude Diagram of the candidate stars from Figure 8. Stars are color-coded based on their derived masses using observed ν_{\max} from `pySYD` and scaling relations from [S. Hekker \(2019\)](#).

two. We choose to derive mass and use previously determined values of radius and temperature. The error in each mass measurement is calculated using standard error propagation and 1σ deviations of ν_{\max} derived using `pySYD`. In Figure 12, the derived stellar masses of the two early M dwarfs, TIC 240764948 and TIC 406430692, are $0.23 \pm 0.03 M_{\odot}$ and $0.23 \pm 0.04 M_{\odot}$. These two masses are the same up to two significant digits because their ν_{\max} are very close due to their proximity in the CMD. The two main sequence K dwarfs, TIC 84332248 and TIC 34115230, were found to have masses of ν_{\max} to be $0.70 \pm 0.10 M_{\odot}$ and $0.86 \pm 0.13 M_{\odot}$. TIC 36596946, which lies very close to ϵ Ind in Figure 8, was found to have a mass of $0.69^{+0.10} M_{\odot}$, which is consistent with the typical stellar mass for this location in the CMD. Finally, the two slightly evolved K dwarfs, TIC 83489517 and TIC 402363298 were found to have stellar masses of $0.75 \pm 0.11 M_{\odot}$ and $0.82 \pm 0.12 M_{\odot}$, respectively. For an estimate of the derived stellar masses for the rest of the candidates, please refer to the color bar of Figure 12. The derived stellar masses using observed frequencies of maximum oscillation (ν_{\max}) and position in the color-magnitude diagram are consistent with our hypothesis for the reason of oscillations. Therefore, this provides a consistency check for our candidate stars and make them more interesting for follow-up observations that might be able to confirm their candidacy.

6. CONCLUSION

In this study, we developed a convolutional autoencoder to identify solar-like oscillations primarily in main-sequence cool dwarf stars using TESS 120 s cadence

data. The network consists of two principal components: an autoencoder, which learns and compresses the morphological features of the input signal into a lower-dimensional representation, and a classifier, which assigns a label based on the compressed features. This architecture was originally adapted from [B. J. Ricketts et al. \(2023\)](#), but was substantially modified for the purposes of this work. In particular, we deepened the network, incorporated attention mechanisms, implemented pooling layers for dimensionality reduction within the encoder, and employed bicubic interpolation for upsampling in the decoder. Furthermore, we used periodograms binned in logarithmic frequency space as input to the network, as this representation highlights the characteristic morphology of solar-like oscillations—combining the low-frequency granulation slope with the Gaussian-like power excess associated with the oscillation envelope.

We trained the network on a catalog of known solar like oscillator from [E. Hatt et al. \(2023\)](#). Other types of variable and non variable stars were taken from [L. A. Balona \(2023\)](#) to make the neural network robust against a diverse class of variable signals. We found that our neural network achieves a validation accuracy of 99.8%.

We used the trained network to find solar-like oscillation signals in new targets from the Asteroseismic Target List ([D. Hey et al. 2024](#)). We found 3463 stars that were flagged as solar-like oscillator by the neural network with a probability higher than 0.5. We next used the `pySYD` package to calculate ν_{\max} , background corrected power spectrum, autocorrelation function and échelle diagram. We shortlisted our candidate list based on (1) consistency of observed ν_{\max} with prediction from scaling relation, (2) periodic autocorrelation function, (3) no contamination from light of background stars, and (4) vertical ridges in échelle diagram. After applying these four cuts, we were left with 24 stars that we propose as candidates to exhibit solar like oscillation. A complete list of these candidates are available in Table 5 and shown in Figure 8. Given the low SNR of these candidates, we need follow-up observations to confirm the existence of solar-like oscillations.

Among the stars analyzed in this study, TIC 240764948 and TIC 406430692 are M-dwarf candidates that satisfy all detection criteria for solar-like oscillations. Both objects lie slightly above the main sequence in the radius-effective temperature plane, which could result from the existence of unresolved equal-mass binary companions in these systems. TIC 240764948 has a nearby companion with nearly identical effective temperature, proper motion, and parallax, indi-

cating that it is likely part of an M-dwarf binary system. Two additional candidates TIC 84332248, and TIC 34115230—are K-dwarf main-sequence stars positioned near previously identified solar-like oscillators in the radius-temperature plot. TIC 95565042, a late main-sequence G-dwarf, is of particular interest because only two TESS detections of solar-like oscillations have been reported at lower temperatures. Finally, TIC 83489517 and TIC 402363298 appear to be slightly evolved K-dwarfs that have begun ascending the subgiant branch. These two objects are especially intriguing, as no prior TESS asteroseismic detections have been reported in this region of the color–magnitude diagram.

In summary, this work shows the power of deep-learning models to identify signals in light-curves that might be missed by visual inspection only. It has the potential of extending the detection limits of TESS 2 min cadence observations, given that we confirm the candidates in follow-up studies, by identifying solar-like oscillator candidates that were previously accessible only through substantially more resource-intensive techniques such as radial velocity measurements. Several of the detected candidates occupy regions of the color–magnitude diagram where TESS asteroseismic detections have so far been rare, underscoring the significance of this sample. The candidate list presented here provides valuable targets for future radial velocity and higher cadence photometry follow-up observations, which are better suited to detect high-frequency, low-amplitude oscillations that may remain unresolved in TESS 2 min data.

ACKNOWLEDGMENTS

This research was partially funded through the Caltech-JPL President’s and Director’s Research & Development Fund Program. This paper includes data collected by the TESS mission. Funding for the TESS mission is provided by the NASA’s Science Mission Directorate. This paper includes data collected with the TESS mission, obtained from the MAST data archive at the Space Telescope Science Institute (STScI) (R. A. Shaw et al. 2025). Funding for the TESS mission is provided by the NASA Explorer Program. STScI is operated by the Association of Universities for Research in Astronomy, Inc., under NASA contract NAS 5–26555. I also sincerely acknowledge May G. Pedersen’s comment and feedback on our analysis and candidate selection. We also sincerely acknowledge Greg Hallinan’s support towards this study during the summer of 2024, and William Chaplin and Sarbani Basu’s support in devising this project.

AUTHOR CONTRIBUTIONS

W. K. primarily led the writing, analysis, and interpretation of the paper, and developed the new software tools used in this study. R. K. led the supervision of this project. D. B. provided regular feedback and helped the interpretation of the results. C. G. and J. W. helped with the development of the software tools. J. F. provided guidance and feedback during SURF program. S. N. helped with the comparison between different light curve analysis techniques.

Software: Astropy (Astropy Collaboration et al. 2013, 2018, 2022), Lightkurve (Lightkurve Collaboration et al. 2018), NumPy (C. R. Harris et al. 2020), Pandas (T. pandas development team 2020), Matplotlib (J. D. Hunter 2007), SciPy (P. Virtanen et al. 2020), pySYD (U. Michelucci 2022), echelle (D. Hey & W. Ball 2020), tess_photometry (M. G. Pedersen in prep), PyTorch (A. Paszke et al. 2019)

REFERENCES

- Abdollahi, M., Torabi, N., Raeisi, S., & Rahvar, S. 2022, Iranian Journal of Astronomy and Astrophysics, 9, doi: [10.22128/ijaa.2022.603.1131](https://doi.org/10.22128/ijaa.2022.603.1131)
- Aguirre, C., Pichara, K., & Becker, I. 2018, Monthly Notices of the Royal Astronomical Society, 482, 5078–5092, doi: [10.1093/mnras/sty2836](https://doi.org/10.1093/mnras/sty2836)
- Anders, F., Chiappini, C., Rodrigues, T. S., et al. 2016, Astronomy & Astrophysics, 597, A30, doi: [10.1051/0004-6361/201527204](https://doi.org/10.1051/0004-6361/201527204)
- Appourchaux, T., Chaplin, W. J., García, R. A., et al. 2012, A&A, 543, A54, doi: [10.1051/0004-6361/201218948](https://doi.org/10.1051/0004-6361/201218948)
- Arentoft, T., Kjeldsen, H., Bedding, T. R., et al. 2008, ApJ, 687, 1180, doi: [10.1086/592040](https://doi.org/10.1086/592040)
- Astropy Collaboration, Robitaille, T. P., Tollerud, E. J., et al. 2013, A&A, 558, A33, doi: [10.1051/0004-6361/201322068](https://doi.org/10.1051/0004-6361/201322068)
- Astropy Collaboration, Price-Whelan, A. M., Sipőcz, B. M., et al. 2018, AJ, 156, 123, doi: [10.3847/1538-3881/aabc4f](https://doi.org/10.3847/1538-3881/aabc4f)

- Astropy Collaboration, Price-Whelan, A. M., Lim, P. L., et al. 2022, *ApJ*, 935, 167, doi: [10.3847/1538-4357/ac7c74](https://doi.org/10.3847/1538-4357/ac7c74)
- Audenaert, J., Kuzlewicz, J. S., Handberg, R., et al. 2021, *AJ*, 162, 209, doi: [10.3847/1538-3881/ac166a](https://doi.org/10.3847/1538-3881/ac166a)
- Audenaert, J., Hon, M., Jayaraman, R., et al. 2025, in *Astronomical Society of the Pacific Conference Series*, Vol. 541, Astronomical Society of the Pacific Conference Series, ed. A. Jacques, R. Seaman, N. Gandilo, & T. Linder, 181, doi: [10.26624/RXGX7087](https://doi.org/10.26624/RXGX7087)
- Baglin, A., Auvergne, M., Boisnard, L., et al. 2006, in 36th COSPAR Scientific Assembly, Vol. 36, 3749
- Balona, L. A. 2023, Identification and classification of TESS variable stars, <https://arxiv.org/abs/2212.10776>
- Bassi, S., Sharma, K., & Gomekar, A. 2021, *Frontiers in Astronomy and Space Sciences*, 8, 168, doi: [10.3389/fspas.2021.718139](https://doi.org/10.3389/fspas.2021.718139)
- Becker, I., Pichara, K., Catelan, M., et al. 2020, *Monthly Notices of the Royal Astronomical Society*, 493, 2981–2995, doi: [10.1093/mnras/staa350](https://doi.org/10.1093/mnras/staa350)
- Bedding, T. R., Huber, D., Stello, D., et al. 2010, *ApJL*, 713, L176, doi: [10.1088/2041-8205/713/2/L176](https://doi.org/10.1088/2041-8205/713/2/L176)
- Benkő, J. M., Szabó, R., Derekas, A., & Sódor, Á. 2016, *MNRAS*, 463, 1769, doi: [10.1093/mnras/stw2136](https://doi.org/10.1093/mnras/stw2136)
- Boyle, A. W., Mann, A. W., & Bush, J. 2025, *ApJ*, 985, 233, doi: [10.3847/1538-4357/adcecc](https://doi.org/10.3847/1538-4357/adcecc)
- Bruntt, H., & Buzasi, D. L. 2006, *Mem. Soc. Astron. Italiana*, 77, 278, doi: [10.48550/arXiv.astro-ph/0509444](https://doi.org/10.48550/arXiv.astro-ph/0509444)
- Burhanudin, U. F., Maund, J. R., Killestein, T., et al. 2021, *Monthly Notices of the Royal Astronomical Society*, 505, 4345–4361, doi: [10.1093/mnras/stab1545](https://doi.org/10.1093/mnras/stab1545)
- Campante, T. L. 2017, *EPJ Web of Conferences*, 160, 01006, doi: [10.1051/epjconf/201716001006](https://doi.org/10.1051/epjconf/201716001006)
- Campante, T. L., Kjeldsen, H., Li, Y., et al. 2024, *A&A*, 683, L16, doi: [10.1051/0004-6361/202449197](https://doi.org/10.1051/0004-6361/202449197)
- Carrier, F., & Eggenberger, P. 2006, *A&A*, 450, 695, doi: [10.1051/0004-6361:20054492](https://doi.org/10.1051/0004-6361:20054492)
- Chaplin, W. J., Elsworth, Y., Davies, G. R., et al. 2014a, *MNRAS*, 445, 946, doi: [10.1093/mnras/stu1811](https://doi.org/10.1093/mnras/stu1811)
- Chaplin, W. J., Kjeldsen, H., Christensen-Dalsgaard, J., et al. 2011, *Science*, 332, 213–216, doi: [10.1126/science.1201827](https://doi.org/10.1126/science.1201827)
- Chaplin, W. J., Basu, S., Huber, D., et al. 2014b, *ApJS*, 210, 1, doi: [10.1088/0067-0049/210/1/1](https://doi.org/10.1088/0067-0049/210/1/1)
- Chontos, A., Huber, D., Sayeed, M., & Yamsiri, P. 2022, *The Journal of Open Source Software*, 7, 3331, doi: [10.21105/joss.03331](https://doi.org/10.21105/joss.03331)
- Christensen-Dalsgaard, J., & Frandsen, S. 1983, *Solar Physics*, 82, 469, doi: [10.1007/BF00872687](https://doi.org/10.1007/BF00872687)
- Gagné, J., Lafrenière, D., Doyon, R., Malo, L., & Artigau, É. 2015, *ApJ*, 798, 73, doi: [10.1088/0004-637X/798/2/73](https://doi.org/10.1088/0004-637X/798/2/73)
- Gaia Collaboration, Prusti, T., de Bruijne, J. H. J., et al. 2016, *A&A*, 595, A1, doi: [10.1051/0004-6361/201629272](https://doi.org/10.1051/0004-6361/201629272)
- Gaia Collaboration, Vallenari, A., Brown, A. G. A., et al. 2023, *A&A*, 674, A1, doi: [10.1051/0004-6361/202243940](https://doi.org/10.1051/0004-6361/202243940)
- Gaulme, P., McKeever, J., Jackiewicz, J., et al. 2016, *ApJ*, 832, 121, doi: [10.3847/0004-637X/832/2/121](https://doi.org/10.3847/0004-637X/832/2/121)
- Guggenberger, E., Hekker, S., Basu, S., & Bellinger, E. P. 2016, *Monthly Notices of the Royal Astronomical Society*, 460, 4277, doi: [10.1093/mnras/stw1326](https://doi.org/10.1093/mnras/stw1326)
- Harris, C. R., Millman, K. J., van der Walt, S. J., et al. 2020, *Nature*, 585, 357, doi: [10.1038/s41586-020-2649-2](https://doi.org/10.1038/s41586-020-2649-2)
- Hatt, E., Nielsen, M. B., Chaplin, W. J., et al. 2023, *A&A*, 669, A67, doi: [10.1051/0004-6361/202244579](https://doi.org/10.1051/0004-6361/202244579)
- Hatt, E. J., Ong, J. M. J., Nielsen, M. B., et al. 2024, *Monthly Notices of the Royal Astronomical Society*, 534, 1060–1076, doi: [10.1093/mnras/stae2053](https://doi.org/10.1093/mnras/stae2053)
- He, K., Zhang, X., Ren, S., & Sun, J. 2015, *Delving Deep into Rectifiers: Surpassing Human-Level Performance on ImageNet Classification*, <https://arxiv.org/abs/1502.01852>
- Hekker, S. 2019, *Scaling relations for solar-like oscillations: a review*, <https://arxiv.org/abs/1907.10457>
- Hey, D., & Ball, W. 2020, *Echelle: Dynamic echelle diagrams for asteroseismology*, 1.4 Zenodo, doi: [10.5281/zenodo.3629933](https://doi.org/10.5281/zenodo.3629933)
- Hey, D., Huber, D., Ong, J., Stello, D., & Foreman-Mackey, D. 2024, *Precise Time-Domain Asteroseismology and a Revised Target List for TESS Solar-Like Oscillators*, <https://arxiv.org/abs/2403.02489>
- Hinton, G. E., & Salakhutdinov, R. R. 2006, *Science*, 313, 504–507, doi: [10.1126/science.1127647](https://doi.org/10.1126/science.1127647)
- Hon, M., Stello, D., & Zinn, J. C. 2018, *The Astrophysical Journal*, 859, 64, doi: [10.3847/1538-4357/aabfdb](https://doi.org/10.3847/1538-4357/aabfdb)
- Hon, M., Huber, D., Kuzlewicz, J. S., et al. 2021, *The Astrophysical Journal*, 919, 131, doi: [10.3847/1538-4357/ac14b1](https://doi.org/10.3847/1538-4357/ac14b1)
- Huber, D., Stello, D., Bedding, T. R., et al. 2009, *Communications in Asteroseismology*, 160, 74, doi: [10.48550/arXiv.0910.2764](https://doi.org/10.48550/arXiv.0910.2764)
- Huber, D., Bedding, T. R., Stello, D., et al. 2010, *ApJ*, 723, 1607, doi: [10.1088/0004-637X/723/2/1607](https://doi.org/10.1088/0004-637X/723/2/1607)
- Huber, D., Bedding, T. R., Stello, D., et al. 2011, *The Astrophysical Journal*, 743, 143, doi: [10.1088/0004-637x/743/2/143](https://doi.org/10.1088/0004-637x/743/2/143)
- Huber, D., Ireland, M. J., Bedding, T. R., et al. 2012, *ApJ*, 760, 32, doi: [10.1088/0004-637X/760/1/32](https://doi.org/10.1088/0004-637X/760/1/32)
- Huber, D., White, T. R., Metcalfe, T. S., et al. 2022, *AJ*, 163, 79, doi: [10.3847/1538-3881/ac3000](https://doi.org/10.3847/1538-3881/ac3000)

- Hunter, J. D. 2007, *Computing in Science and Engineering*, 9, 90, doi: [10.1109/MCSE.2007.55](https://doi.org/10.1109/MCSE.2007.55)
- Jamal, S., & Bloom, J. S. 2020, *The Astrophysical Journal Supplement Series*, 250, 30, doi: [10.3847/1538-4365/aba8ff](https://doi.org/10.3847/1538-4365/aba8ff)
- Jenkins, J. M., Twicken, J. D., McCauliff, S., et al. 2016, in *Society of Photo-Optical Instrumentation Engineers (SPIE) Conference Series*, Vol. 9913, *Software and Cyberinfrastructure for Astronomy IV*, ed. G. Chiozzi & J. C. Guzman, 99133E, doi: [10.1117/12.2233418](https://doi.org/10.1117/12.2233418)
- Kallinger, T., De Ridder, J., Hekker, S., et al. 2014, *A&A*, 570, A41, doi: [10.1051/0004-6361/201424313](https://doi.org/10.1051/0004-6361/201424313)
- Karim, W. M. Z., Kiman, R., Hallinan, G., et al. 2025, in *American Astronomical Society Meeting Abstracts*, Vol. 245, *American Astronomical Society Meeting Abstracts #245*, 111.04
- Kim, G. I., & Chung, K. 2024, *Sensors (Basel)*, 24, 6402, doi: [10.3390/s24196402](https://doi.org/10.3390/s24196402)
- Kingma, D. P., & Ba, J. 2014, arXiv preprint arXiv:1412.6980
- Kinoshita, Y., & Kiya, H. 2020, Fixed smooth convolutional layer for avoiding checkerboard artifacts in CNNs, <https://arxiv.org/abs/2002.02117>
- Kjeldsen, H., Bedding, T. R., Arentoft, T., et al. 2008, *ApJ*, 682, 1370, doi: [10.1086/589142](https://doi.org/10.1086/589142)
- Koch, D. G., Borucki, W. J., Basri, G., et al. 2010, *The Astrophysical Journal*, 713, L79–L86, doi: [10.1088/2041-8205/713/2/179](https://doi.org/10.1088/2041-8205/713/2/179)
- Lagarde, N., Miglio, A., Eggenberger, P., et al. 2015, *A&A*, 580, A141, doi: [10.1051/0004-6361/201525856](https://doi.org/10.1051/0004-6361/201525856)
- Lebreton, Y., & Goupil, M. J. 2014, *A&A*, 569, A21, doi: [10.1051/0004-6361/201423797](https://doi.org/10.1051/0004-6361/201423797)
- LeCun, Y., Bottou, L., Bengio, Y., & Haffner, P. 1998, *Proceedings of the IEEE*, 86, 2278, doi: [10.1109/5.726791](https://doi.org/10.1109/5.726791)
- Lightkurve Collaboration, Cardoso, J. V. d. M., Hedges, C., et al. 2018, *Lightkurve: Kepler and TESS time series analysis in Python*, *Astrophysics Source Code Library* <http://ascl.net/1812.013>
- Lomb, N. R. 1976, *Ap&SS*, 39, 447, doi: [10.1007/BF00648343](https://doi.org/10.1007/BF00648343)
- Lund, M. N., Chontos, A., Grundahl, F., et al. 2025, *A&A*, 701, A285, doi: [10.1051/0004-6361/202555485](https://doi.org/10.1051/0004-6361/202555485)
- Mahabal, A., Sheth, K., Gieseke, F., et al. 2017, in 2017 *IEEE Symposium Series on Computational Intelligence (SSCI) (IEEE)*, 1–8, doi: [10.1109/ssci.2017.8280984](https://doi.org/10.1109/ssci.2017.8280984)
- Marasco, C., Tayar, J., & Nidever, D. 2025, *Asteroseismology of Metal-Poor Red Giants Observed by TESS*, <https://arxiv.org/abs/2504.18642>
- Mathur, S., García, R. A., Bugnet, L., et al. 2019, *Frontiers in Astronomy and Space Sciences*, 6, doi: [10.3389/fspas.2019.00046](https://doi.org/10.3389/fspas.2019.00046)
- Mathur, S., García, R. A., Régulo, C., et al. 2010, *A&A*, 511, A46, doi: [10.1051/0004-6361/200913266](https://doi.org/10.1051/0004-6361/200913266)
- Mathur, S., Huber, D., Batalha, N. M., et al. 2017, *ApJS*, 229, 30, doi: [10.3847/1538-4365/229/2/30](https://doi.org/10.3847/1538-4365/229/2/30)
- Mathur, S., García, R. A., Breton, S., et al. 2022, *A&A*, 657, A31, doi: [10.1051/0004-6361/202141168](https://doi.org/10.1051/0004-6361/202141168)
- Metcalf, T. S., Monteiro, M. J. P. F. G., Thompson, M. J., et al. 2010, *ApJ*, 723, 1583, doi: [10.1088/0004-637X/723/2/1583](https://doi.org/10.1088/0004-637X/723/2/1583)
- Metcalf, T. S., Chaplin, W. J., Appourchaux, T., et al. 2012, *The Astrophysical Journal*, 748, L10, doi: [10.1088/2041-8205/748/1/110](https://doi.org/10.1088/2041-8205/748/1/110)
- Metcalf, T. S., Creevey, O. L., Doğan, G., et al. 2014, *ApJS*, 214, 27, doi: [10.1088/0067-0049/214/2/27](https://doi.org/10.1088/0067-0049/214/2/27)
- Michelucci, U. 2022, *An Introduction to Autoencoders*, <https://arxiv.org/abs/2201.03898>
- Mosser, B., Elsworth, Y., Hekker, S., et al. 2012, *A&A*, 537, A30, doi: [10.1051/0004-6361/20111735210.1086/141952](https://doi.org/10.1051/0004-6361/20111735210.1086/141952)
- Murphy, S. J., Shibahashi, H., & Kurtz, D. W. 2013, *MNRAS*, 430, 2986, doi: [10.1093/mnras/stt105](https://doi.org/10.1093/mnras/stt105)
- Naul, B., Bloom, J. S., Pérez, F., & van der Walt, S. 2017, *Nature Astronomy*, 2, 151–155, doi: [10.1038/s41550-017-0321-z](https://doi.org/10.1038/s41550-017-0321-z)
- Nielsen, M. B., Davies, G. R., Ball, W. H., et al. 2025, *PBJam: Automating asteroseismology of solar-like oscillators*, *Astrophysics Source Code Library*, record ascl:2504.002 <http://ascl.net/2504.002>
- pandas development team, T. 2020, *pandas-dev/pandas: Pandas*, latest Zenodo, doi: [10.5281/zenodo.3509134](https://doi.org/10.5281/zenodo.3509134)
- Paszke, A., Gross, S., Massa, F., et al. 2019, *PyTorch: An Imperative Style, High-Performance Deep Learning Library*, <https://arxiv.org/abs/1912.01703>
- Pecaut, M. J., & Mamajek, E. E. 2013, *ApJS*, 208, 9, doi: [10.1088/0067-0049/208/1/9](https://doi.org/10.1088/0067-0049/208/1/9)
- Pérez-Galarce, F., Martínez-Palomera, J., Pichara, K., Huijse, P., & Catelan, M. 2025, *A self-regulated convolutional neural network for classifying variable stars*, <https://arxiv.org/abs/2505.14877>
- Ricker, G. R., Winn, J. N., Vanderspek, R., et al. 2015, *Journal of Astronomical Telescopes, Instruments, and Systems*, 1, 014003, doi: [10.1117/1.JATIS.1.1.014003](https://doi.org/10.1117/1.JATIS.1.1.014003)
- Ricketts, B. J., Steiner, J. F., Garraffo, C., Remillard, R. A., & Huppenkothen, D. 2023, *Monthly Notices of the Royal Astronomical Society*, 523, 1946–1966, doi: [10.1093/mnras/stad1332](https://doi.org/10.1093/mnras/stad1332)
- Rodríguez-López, C. 2019, *Frontiers in Astronomy and Space Sciences*, 6, 76, doi: [10.3389/fspas.2019.00076](https://doi.org/10.3389/fspas.2019.00076)

- Rodríguez-López, C., Gizis, J. E., MacDonald, J., Amado, P. J., & Carosso, A. 2014, *Monthly Notices of the Royal Astronomical Society*, 446, 2613–2620, doi: [10.1093/mnras/stu2211](https://doi.org/10.1093/mnras/stu2211)
- Rodríguez-López, C., MacDonald, J., & Moya, A. 2012, *Monthly Notices of the Royal Astronomical Society: Letters*, 419, L44–L48, doi: [10.1111/j.1745-3933.2011.01174.x](https://doi.org/10.1111/j.1745-3933.2011.01174.x)
- Rumelhart, D. E., Hinton, G. E., & Williams, R. J. 1986, *Nature*, 323, 533, doi: [10.1038/323533a0](https://doi.org/10.1038/323533a0)
- Sayed, M., Huber, D., Chontos, A., & Li, Y. 2025, A Homogeneous Catalog of Oscillating Solar-Type Stars Observed by the Kepler Mission and a New Amplitude Scaling Relation Including Chromospheric Activity, <https://arxiv.org/abs/2503.15599>
- Schofield, M., Chaplin, W. J., Huber, D., et al. 2019, *The Astrophysical Journal Supplement Series*, 241, 12, doi: [10.3847/1538-4365/ab04f5](https://doi.org/10.3847/1538-4365/ab04f5)
- Shaw, R. A., Novacescu, J. L., Weissman, S., et al. 2025, The Impact of the MAST Data Archive, <https://arxiv.org/abs/2512.18101>
- Silva Aguirre, V., Casagrande, L., Basu, S., et al. 2012, *ApJ*, 757, 99, doi: [10.1088/0004-637X/757/1/99](https://doi.org/10.1088/0004-637X/757/1/99)
- Simonyan, K., & Zisserman, A. 2015, Very Deep Convolutional Networks for Large-Scale Image Recognition, <https://arxiv.org/abs/1409.1556>
- Stassun, K. G., Oelkers, R. J., Pepper, J., et al. 2018, *AJ*, 156, 102, doi: [10.3847/1538-3881/aad050](https://doi.org/10.3847/1538-3881/aad050)
- Teixeira, T. C., Kjeldsen, H., Bedding, T. R., et al. 2009, *A&A*, 494, 237, doi: [10.1051/0004-6361:200810746](https://doi.org/10.1051/0004-6361:200810746)
- Valentini, M., Chiappini, C., Miglio, A., et al. 2016, *Astronomische Nachrichten*, 337, 970–975, doi: [10.1002/asna.201612399](https://doi.org/10.1002/asna.201612399)
- VanderPlas, J. T. 2018, *ApJS*, 236, 16, doi: [10.3847/1538-4365/aab766](https://doi.org/10.3847/1538-4365/aab766)
- Vaswani, A., Shazeer, N., Parmar, N., et al. 2017, in *Advances in Neural Information Processing Systems (NeurIPS)*, 5998–6008
- Virtanen, P., Gommers, R., Oliphant, T. E., et al. 2020, *Nature Medicine*, 17, 261, doi: [10.1038/s41592-019-0686-2](https://doi.org/10.1038/s41592-019-0686-2)
- Walker, G., Matthews, J., Kuschnig, R., et al. 2003, *PASP*, 115, 1023, doi: [10.1086/377358](https://doi.org/10.1086/377358)
- Yu, F., & Koltun, V. 2016, Multi-Scale Context Aggregation by Dilated Convolutions, <https://arxiv.org/abs/1511.07122>
- Yu, J., Huber, D., Bedding, T. R., et al. 2018, *ApJS*, 236, 42, doi: [10.3847/1538-4365/aaaf74](https://doi.org/10.3847/1538-4365/aaaf74)
- Yıldız, M., Çelik Orhan, Z., & Kayhan, C. 2019, *Monthly Notices of the Royal Astronomical Society*, 489, 1753–1769, doi: [10.1093/mnras/stz2223](https://doi.org/10.1093/mnras/stz2223)
- Zhang, K., & Bloom, J. S. 2021, *MNRAS*, 505, 515, doi: [10.1093/mnras/stab1248](https://doi.org/10.1093/mnras/stab1248)

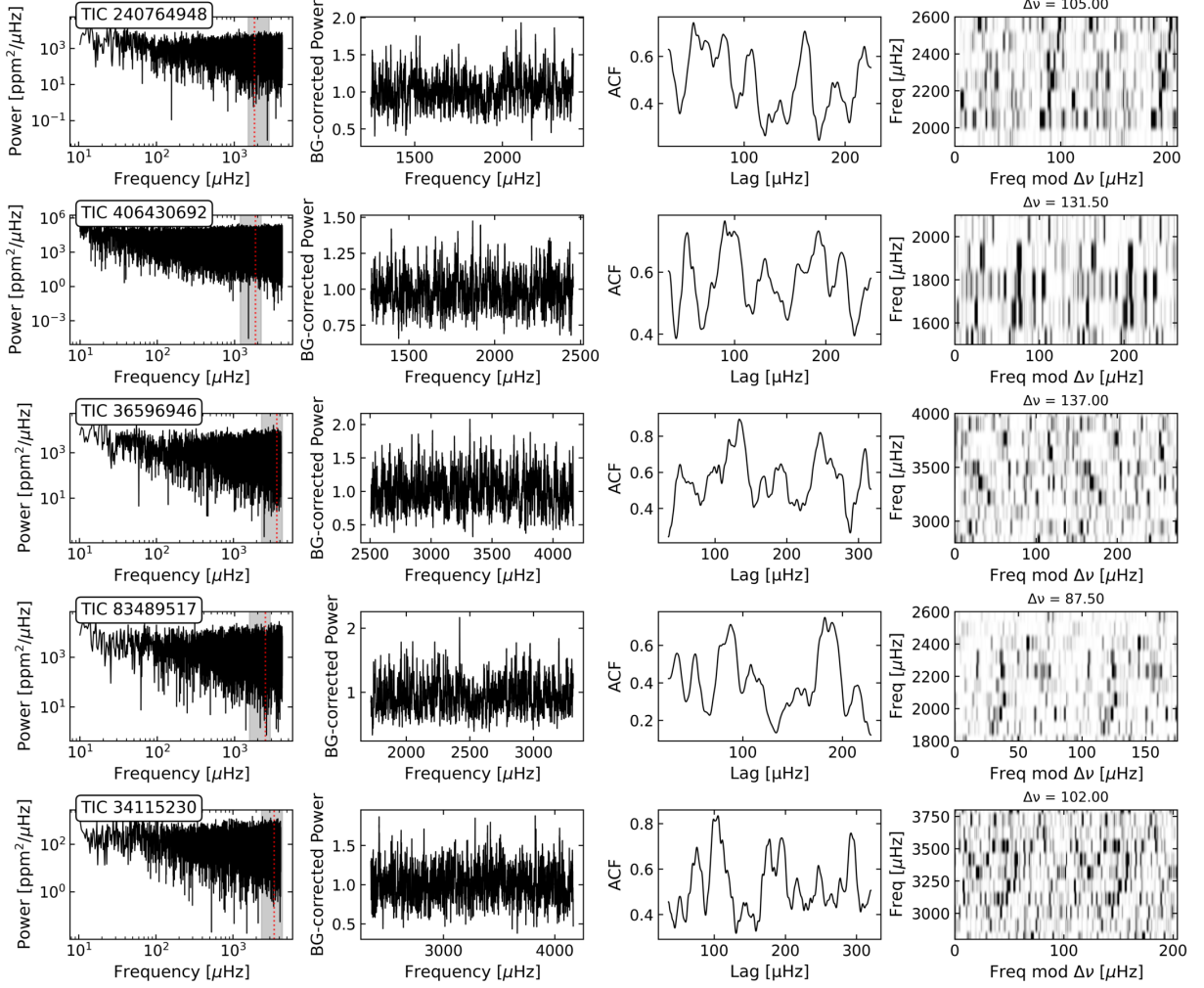


Figure 13. Diagnostic plots of TIC 240764948, TIC 406430692, TIC 36596946, TIC 83489517, and TIC 34115230. *First Column:* power spectrum with region near observed ν_{\max} is shaded in dark grey and predicted ν_{\max} from scaling relation in dotted red line, *Second Column:* background-corrected power spectrum zoomed-in on expected ν_{\max} , *Third Column:* auto-correlation function, *Fourth Column:* échelle diagram. The plots are in ascending order of temperature. The objects are presented in ascending order of temperature.

7. APPENDIX

7.1. Diagnostic Plots for Candidates

In this section, we present the diagnostic plot containing power spectrum, background-corrected power spectrum, autocorrelation function, and échelle diagram of all the candidates in Figure 8 that were not shown in Figure 7.

7.2. Neural Network

The neural network used in this study is composed of two main component: autoencoder and the classifier. The architecture of both these networks were discussed in great detail in Section 3. Here, we present a diagram of the encoder architecture, and the architecture of the classifier is the same as the classification network described in S. Jamal & J. S. Bloom (2020).

7.2.1. Autoencoder Architecture

The autoencoder is comprised of an encoder and a decoder. As described in Section 3.1, the encoder network compresses the input signal of size 4096 down to 128 in the latent space. It is comprised of convolutional and dense

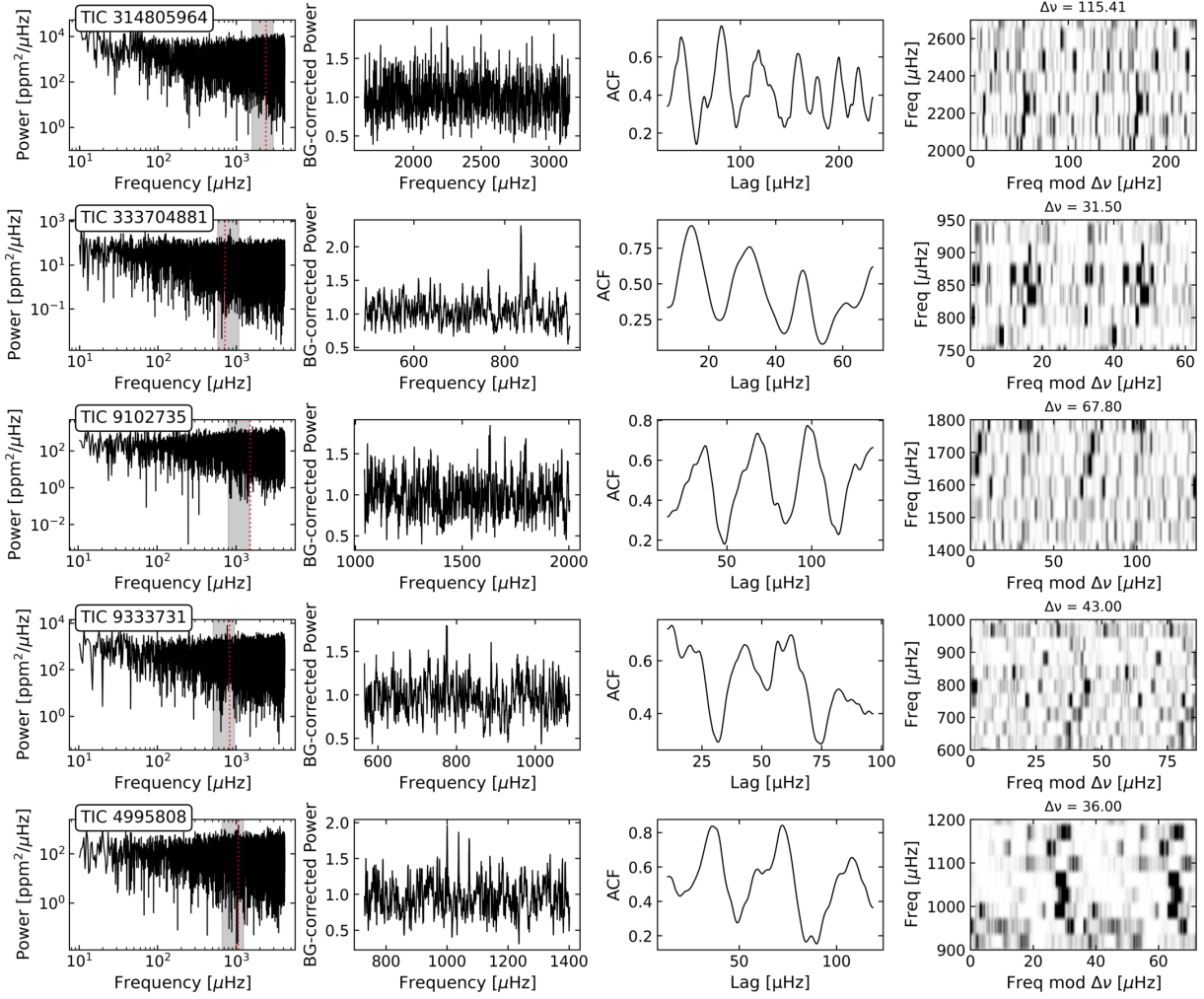


Figure 14. The same as at Figure 10, but for TIC 314805964, TIC 333704881, TIC 9102735, TIC 9333731, and TIC 4995808.

layers that learn the features of input signal and pooling layers that compresses the signal to a lower dimension. The detailed architecture of the encoder network is presented in Figure 17.

The decoder is a mirror copy of encoder, except all the pooling layers are substituted by interpolation layers to reconstruct the original input length from low-dimensional latent space. To see the network hyperparameters used for training and description of each layers, please refer to Section 3.

7.3. Latent Space Comparison

Here, we present a comparison between the latent space representations of solar-like oscillators and other classes of stellar variability. The autoencoder described in Section 3 takes a power spectrum binned to 4096 points as input, compresses this information into a 128-dimensional latent space, and passes this low-dimensional representation to the classifier. This latent representation effectively encodes salient frequency-domain features that enable discrimination between solar-like oscillators and other types of variables.

To verify the claim that latent space encodes features that discriminate solar-like oscillators from other types of variables, we have looked at the latent space representation of several solar-like oscillators and other types of variables from our validation set. The key distinguishing feature of solar-like oscillators in the latent space was the existence of 4 or more high-SNR peaks, while other types of variables usually had one or two high-SNR peaks followed by a cluster of low SNR peaks. An illustrative example is shown in Figure 18, where we can notice the solar-like oscillator has 4 high-SNR peaks, whereas the NonSOLR class has usually one high-SNR peak followed by a groups of small peaks.

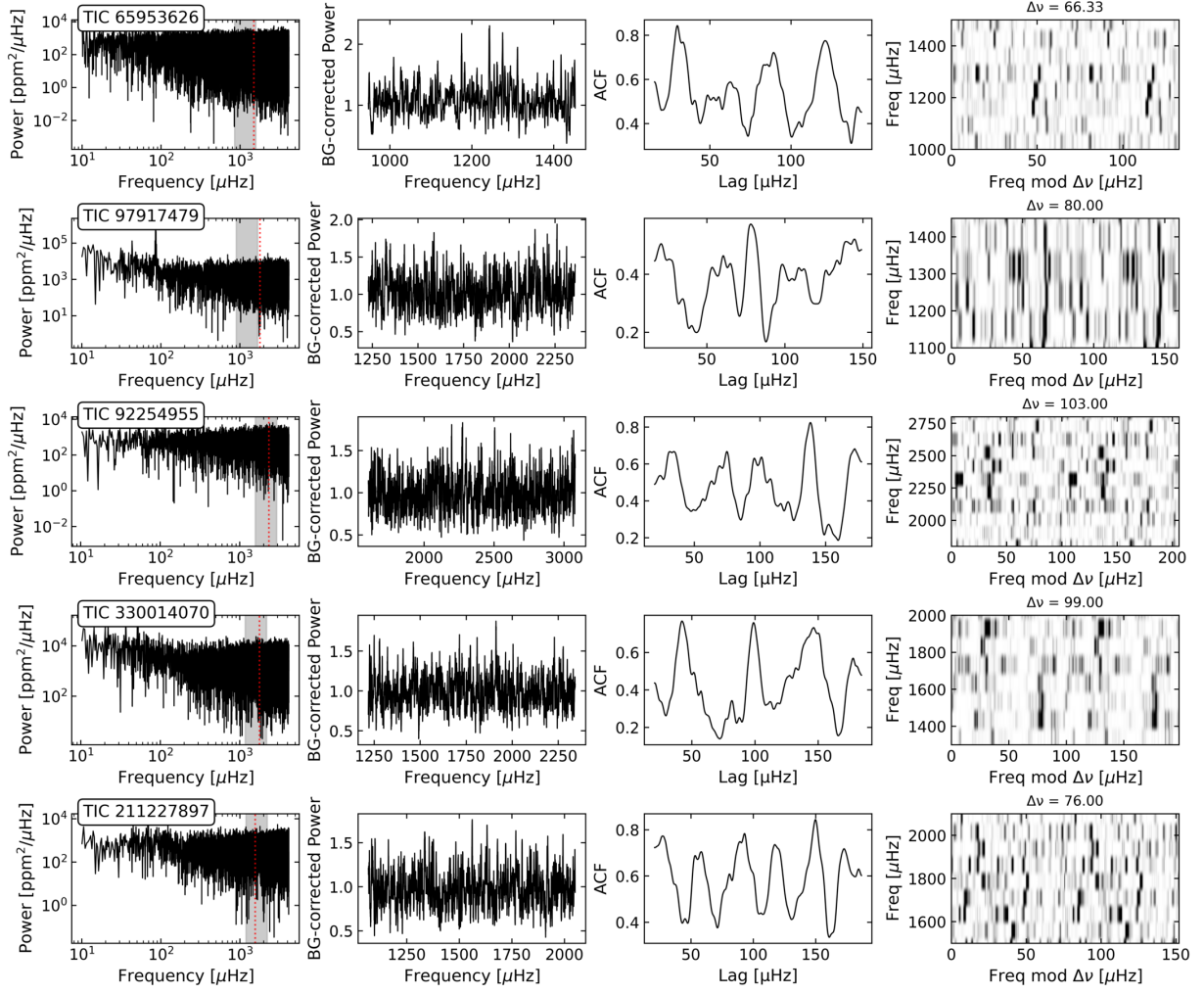


Figure 15. The same as at Figure 10, but for TIC 65953626, TIC 97917479, TIC 92254955, TIC 330014070, TIC 211227897.

This observation was consistent throughout the sample of latent spaces we have manually checked for different stars of these SOLR and NonSOLR classes.

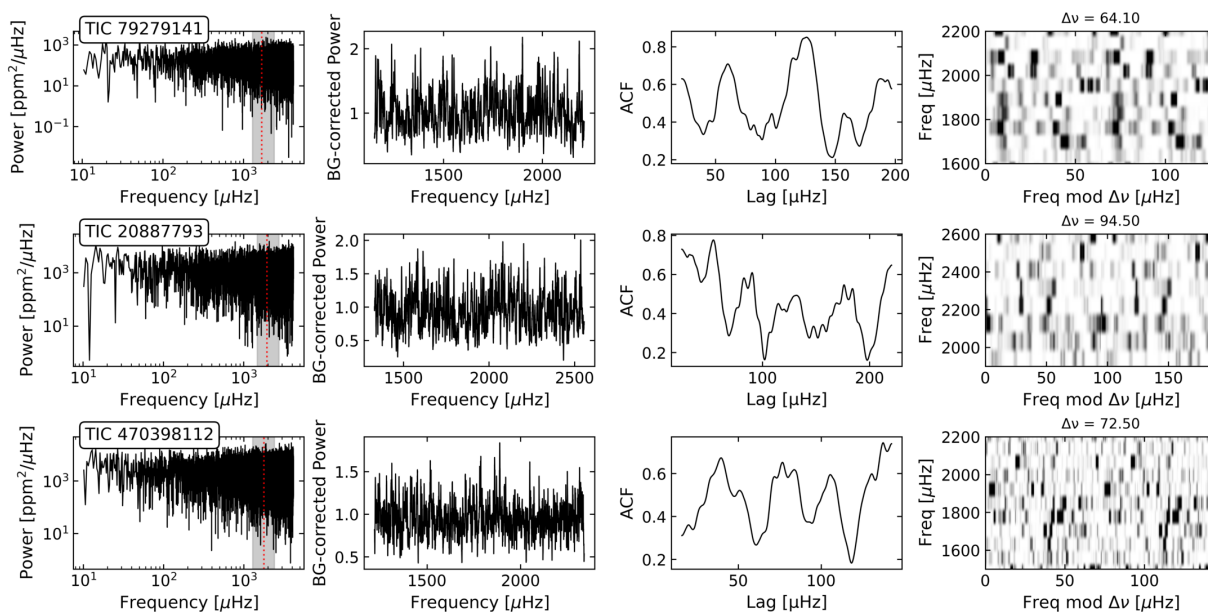


Figure 16. The same at at Figure 10, but for TIC 79279141, TIC 20887793, and TIC 470398112.

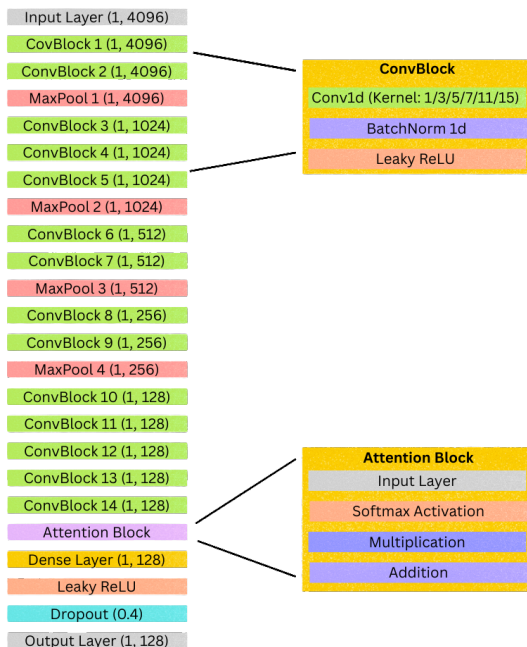


Figure 17. Detailed architecture of the encoder network

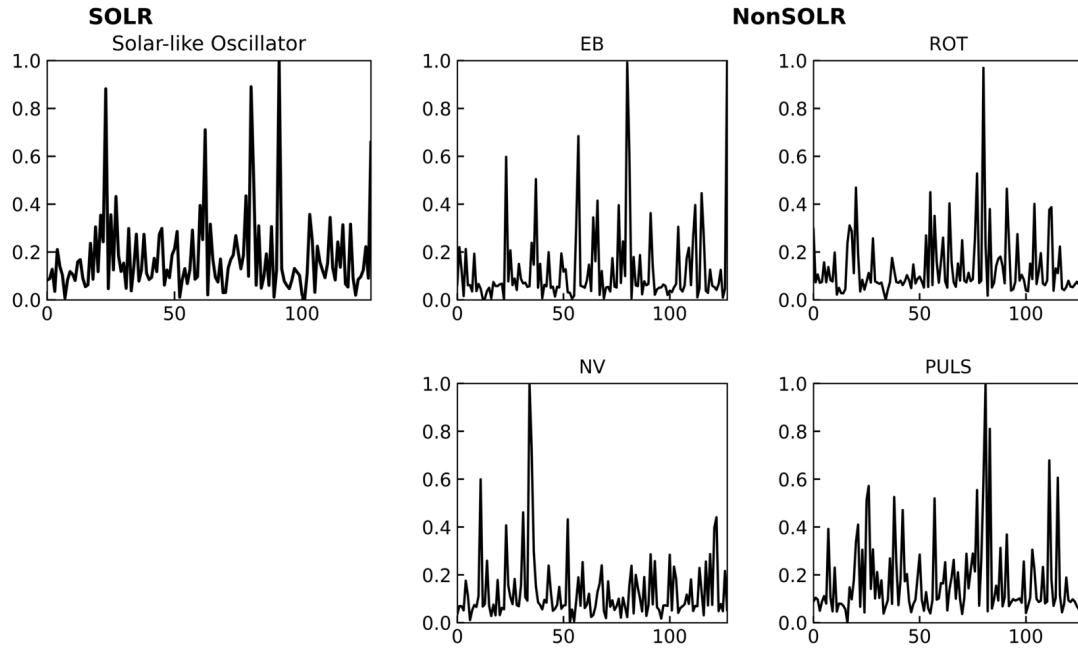


Figure 18. Comparison of latent space representation between a solar-like oscillator and other types of variables. The SOLR column represents solar-like oscillation and NonSOLR column represents other types of variables. All signals are normalized between 0 and 1.